
Rethinking Model Re-Basin and Linear Mode Connectivity

Xingyu Qu

`xingyu.qu@mbzuai.ac.ae`

Mohamed bin Zayed University of Artificial Intelligence (MBZUAI)

Samuel Horvath

`samuel.horvath@mbzuai.ac.ae`

Mohamed bin Zayed University of Artificial Intelligence (MBZUAI)

Abstract

Recent studies suggest that with sufficiently wide models, most SGD solutions can, up to permutation, converge into the same basin. This phenomenon, known as the *model re-basin* regime, has significant implications for model averaging by ensuring the *linear mode connectivity*. However, current re-basin strategies are ineffective in many scenarios due to a lack of comprehensive understanding of underlying mechanisms. Addressing this gap, this paper provides novel insights into understanding and improving the standard practice. Firstly, we decompose re-normalization into rescaling and reshift, uncovering that rescaling plays a crucial role in re-normalization while re-basin performance is sensitive to shifts in model activation. The finding calls for a more nuanced handling of the activation shift. Secondly, we identify that the merged model suffers from the issue of *activation collapse* and *magnitude collapse*. Varying the learning rate, weight decay, and initialization method can mitigate the issues and improve model performance. Lastly, we propose a new perspective to unify the re-basin and pruning, under which a lightweight yet effective post-pruning technique is derived, which can significantly improve the model performance after pruning. Our implementation is available at <https://github.com/XingyuQu/rethink-re-basin>.

1 Introduction and Related Work

Model merging – averaging multiple models in the weight space, can often produce a single model that combines the strengths of all individual models [31, 58, 48, 28]. A successful model merging is indeed equivalent to the existence of *linear mode connectivity (LMC)* [19], i.e., there is no barrier between the selected models on the loss landscape. However, a significant barrier generally exists between independently trained models, hindering the general application of model merging [19, 44]. A recent line of research around *model re-basin* sheds light on resolving this issue by revealing that the permutation invariance of neural networks and specific re-normalization strategies can mitigate the barrier, hence creating space for effective merging [3, 14, 32, 59]. We summarize the standard approach in Figure 1. Yet, current re-basin practices are still ineffective in many aspects, e.g. an impractical model width is often necessary to guarantee the performance [3]. One reason for this unsatisfactory development is the limited understanding of the field thus far. Although a few works have provided preliminary analysis, they primarily address simpler and more idealized scenarios, lacking practical guidelines for broader application [14, 15].

Contributions. This paper conducts an in-depth review of the standard practice through empirical exploration, providing novel insights into understanding and improving model re-basin and linear

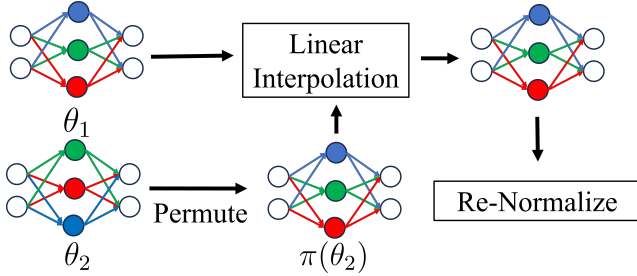


Figure 1: The standard approach of model re-basin. Given two networks θ_1 and θ_2 , a matching algorithm is first performed to find a proper permutation π that maximizes some “similarity” between θ_1 and $\pi(\theta_2)$. The two models, after matching, are then merged by linear interpolation. Meanwhile, certain re-normalization strategies applied to the merged model are found to be important in guaranteeing the model performance.

mode connectivity. As the first work of this kind, we focus on the fundamental setup of matching independently trained models that share the same architecture and are trained on the same dataset. The main contributions are summarized below.

- **Re-Normalization.** We decompose the re-normalization as *rescaling* and *reshift*, empirically uncovering that rescaling plays the main role in REPAIR while the re-basin performance is sensitive to shifts in model activation. Removing the activation shift in REPAIR or model architectures sometimes significantly reduces the barrier. Our results highlight the necessity for more nuanced approaches to handling the activation shifts in re-basin practices.
- **Matching.** We identify the issue of *activation collapse* and *magnitude collapse* in the merged model. By analyzing and mitigating the irregularities, we unveil the impact of learning rate, weight decay, and initialization strategy on the barrier and re-basin performance.
- **Re-Basin and Pruning.** We propose a novel perspective to unify model re-basin and pruning practices, under which a lightweight yet effective post-pruning technique is derived. Extensive experimental results verified its ability to improve the model performance after pruning significantly.

2 Preliminaries

Terminology. We clarify some terminologies used in the paper. Most discussions focus on the linear interpolation between two trained models θ_1, θ_2 on the loss/error landscape. We will call θ_1, θ_2 the *end models*, and the interpolated model θ_λ ($\lambda \in [0, 1]$) the *merged model*. Especially, the merged model at the middle ($\lambda = 1/2$) is named *midpoint model*. The *barrier* or *normalized barrier* between two end models is studied. When some matching algorithm is applied, we add the *post-matching* prefix if necessary, e.g., post-matching midpoint model, post-matching barrier. Similar terminologies are used for specific metrics, e.g., the post-matching midpoint accuracy is the accuracy of the post-matching midpoint model. Regarding model architecture, we use the shorter form *BatchNorm/BN* and *LayerNorm/LN* for batch normalization and layer normalization. Models without normalization layers are sometimes called *plain models*. We often use the shorter form *WM* and *AM* for weight and activation matching, respectively. Lastly, the x-axis λ in many plots is the interpolation coefficient as in Definition 2.1.

2.1 Barrier and Linear Mode Connectivity

Definition 2.1 ((Normalized) Loss barrier). Given two models $\theta_1, \theta_2 \in \Theta$, and the loss function \mathcal{L} such that $\mathcal{L}(\theta_1) \approx \mathcal{L}(\theta_2)$, the *loss barrier* between θ_1 and θ_2 is defined as $\mathcal{B}(\theta_1, \theta_2) := \max_{\lambda \in [0, 1]} \mathcal{L}((1 - \lambda)\theta_1 + \lambda\theta_2) - (1 - \lambda)\mathcal{L}(\theta_1) - \lambda\mathcal{L}(\theta_2)$. Furthermore, given a re-normalization operation $r : \Theta \rightarrow \Theta$, the *normalized loss barrier* between θ_1 and θ_2 subject to r is defined as $\mathcal{B}_r(\theta_1, \theta_2) := \max_{\lambda \in [0, 1]} \mathcal{L}(r((1 - \lambda)\theta_1 + \lambda\theta_2)) - (1 - \lambda)\mathcal{L}(\theta_1) - \lambda\mathcal{L}(\theta_2)$.

The definition of loss barrier follows [32]. It measures the geometry property of the loss landscape between two models. Empirically, the (normalized) barrier mostly occurs in the middle. Prior works have observed that the post-matching barrier could still be large, but the post-matching normalized barrier is small with a proper choice of r [3, 32]. We say there is a *linear mode connectivity* (LMC) between two models if the loss barrier or normalized loss barrier is closed to 0. Similar barrier definitions can be obtained for metrics such as accuracy and error. In [14], the authors conjectured

that LMC generally holds between any pair of SGD solutions with sufficient width if the neural network’s permutation invariance is considered.

2.2 Ingredients of Model Re-Basin

Permutation Invariance [27]. To simplify the explanation, we focus on fully connected feed-forward networks. The statement can be naturally extended to other architectures. For an L -layer multilayer perceptron (MLP), $N(x) = N^{(L)}(x)$, $N^{(i+1)}(x) = \sigma(W_{i+1}N^{(i)}(x) + b_{i+1})$, where $N^{(i)}(x)$ denotes the output of the i th layer, σ denotes the activation function, W_{i+1} and b_{i+1} are the weights and biases of the $(i+1)$ th layer. The *permutation invariance* of a neural network means that if we apply a permutation P to the output of one layer, i.e., $N^{(i)}(x) \leftarrow PN^{(i)}(x)$, the network output remains the same once permute parameters in the next layer accordingly: $W_{i+1} \leftarrow W_{i+1}P^T$, since it holds that $P^T P = I$. Meanwhile, permuting the output of one layer can be achieved by permuting parameters in the layer: $W_i \leftarrow PW_i$, $b_i \leftarrow Pb_i$. Therefore, one can obtain a functionally equivalent network $N'(x) = N(x)$ by applying permutations to the parameters $\theta' = \pi(\theta)$.

Neural network matching aims to align two networks in the parameter space by the permutation invariances [3, 14, 55]. A closely related direction is *model fusion*, where a more general soft-alignment is considered [29, 51]. In this work, we adopt two widely used matching algorithms in the literature: weight matching [3] and activation matching [3, 32]. Briefly, given two networks N_1 and N_2 , weight matching seeks the permutation minimizing the distance between the parameters: $\pi^* = \operatorname{argmin}_\pi \|\theta_1 - \pi(\theta_2)\|$, while activation matching minimizes the distance between intermediate activations of each hidden layer: $\pi^* = \operatorname{argmin}_\pi \sum_i \|N_1^{(i)}(x) - \pi(N_2)^{(i)}(x)\|$. During our exploration, we uncovered notable drawbacks in previous implementations of activation matching and made corresponding improvements. Discussions are given in Appendix F.2.

Re-Normalization. As mentioned in Sec. 2.1, some re-normalization techniques applied to the merged models are often necessary for a good merging, even after permuting the end models. There are three standard re-normalization strategies in the literature:

- **RESET**: For models with BatchNorm layers, reset the BatchNorm statistics in the merged models. Specifically, the running mean and variance in each BatchNorm layer are first reset to default values and then re-accumulated by feeding the entire or a portion of the training dataset to the model.
- **Implicit Normalization**: Previous works noticed that the post-matching barriers between two models with LayerNorm layers are naturally smaller [3, 32]. The intuition is that the model is already implicitly normalized by the running-time normalization in LayerNorm layers.
- **REPAIR** [32]: REPAIR is a generalization of RESET that can be applied to models without BatchNorm layers. We leave the detailed introduction to Sec. 3.1.

2.3 Experimental Setup

Following the standard setup in prior works, we study re-basing independent SGD solutions trained on the same image classification datasets: MNIST [37], CIFAR-10/CIFAR-100 [35]. Pruning results on ImageNet [11] are also provided. We explore various network architectures, including the VGG [49], ResNet [26], and ConvNeXt-T [39] with different depth, width, and the inclusion of BatchNorm [30], LayerNorm [6], and no normalization. ResNet with Fixup [61] initialization is also considered. In most experiments, we first independently train two models and then study the barrier between them after applying matching and certain re-normalization. We follow the standard recipe for network training [19, 26]. We train the VGGs and ResNets for 160 epochs with weight decay 10^{-4} . Unless otherwise specified, the learning rate is initialized at 0.1 and reduced by a factor of 10 at iterations 32,000 and 48,000. A linear warmup or cosine decay is also adopted in some settings to ensure smooth training. Complete experimental details are provided in Appendix D. Results with the error bar are calculated over four random seeds.

3 Rethinking Re-Normalization

In the standard re-basin practice, re-normalization is important to guarantee the quality of merged models when matching algorithms are insufficient. However, understanding of current re-normalization techniques remains limited. In this section, we revisit the re-normalization by a novel rescaling-reshift decomposition, providing evidence that rescaling plays the main role in REPAIR while re-basin performance is sensitive to shifts in model activation. Completely removing the activation shift in

Table 1: Ablation to REPAIR: rescaling is the most important in REPAIR; removing reshift sometimes even helps. Test Accuracy of the post-matching normalized midpoint model between two independent solutions is reported. “-” is the original post-matching midpoint accuracy. In “RESCALE*”, $w_\lambda^{(i,j)}$ in (2) is modified to be the average goal std. $\bar{w}_\lambda^{(i)}$ across all channels in layer i . Weight matching is utilized for VGG16, and activation matching is used for the others. The best results are in bold.

Model	-	REPAIR	RESCALE	RESCALE*	RESHIFT
VGG16	$14.22 \pm 2.27\%$	$75.1 \pm 4.09\%$	$84.32 \pm 0.77\%$	$78.18 \pm 0.88\%$	10 %
Plain ResNet20	$61.42 \pm 2.75\%$	$72.22 \pm 1.82\%$	$72.01 \pm 1.52\%$	$65.81 \pm 3.18\%$	$10.12 \pm 0.21\%$
Fixup ResNet20	$42.81 \pm 0.23\%$	$73.32 \pm 0.15\%$	$71.42 \pm 0.23\%$	$67.26 \pm 0.29\%$	10 %

REPAIR or model architectures sometimes significantly reduces the barrier. The results suggest that activation shift should be treated carefully for a good re-basin.

3.1 Deconstructing REPAIR

Previous Understanding. First, we recall the existing understanding of re-normalization and introduce REPAIR. Jordan et al. [32] firstly connected the unsatisfactory performance of post-matching merged models to the *variance collapse* phenomenon: variances of the hidden activation significantly decrease in the merged models, and this reduction becomes more pronounced in deeper layers. Eventually, it leads to nearly constant activations in the output layer, resulting in model performance degradation. The variance collapse was observed to become less severe in models with LayerNorm and more negligible in models with BatchNorm after applying RESET. This motivated the authors to propose *REPAIR*, which generalizes the idea of *activation statistics correction* in RESET on models of more diverse architectures, including plain models. Given two networks N_1 , N_2 and the merged network N_λ with parameters $\theta_\lambda = (1 - \lambda) \cdot \theta_1 + \lambda \cdot \theta_2$, REPAIR corrects the channel-wise statistics for all channels $\{N_\lambda^{(i,j)}\}$ in selected layers $\{N_\lambda^{(i)}\}$ based on the corresponding channels $\{N_1^{(i,j)}\}, \{N_2^{(i,j)}\}$ from end models:

$$\text{REPAIR: } \tilde{N}_\lambda^{(i,j)}(x) \leftarrow \frac{\tilde{N}_\lambda^{(i,j)}(x) - \mu_\lambda^{(i,j)}}{\sigma_\lambda^{(i,j)}} \cdot w_\lambda^{(i,j)} + b_\lambda^{(i,j)}, \quad (1)$$

where $x, \tilde{N}_\lambda^{(i,j)}(x)$ is the input and pre-activation of $N_\lambda^{(i,j)}$, $w_\lambda^{(i,j)} = (1 - \lambda) \cdot \mu_1^{(i,j)} + \lambda \cdot \mu_2^{(i,j)}$ is the goal standard deviation, $b_\lambda^{(i,j)} = (1 - \lambda) \cdot \sigma_1^{(i,j)} + \lambda \cdot \sigma_2^{(i,j)}$ is the goal activation mean, and $\mu^{(i,j)}$, $\sigma^{(i,j)}$ is the channel-wise mean and standard deviation of the layer output. The subscript refers to which model the statistics belong to, and the superscript (i, j) refers to the j -th channel in the i -th layer. *In short, the current understanding is that re-normalization strategies can make the activation statistics in the merged model similar to the ones in end models to alleviate variance collapse. In particular, the design of REPAIR exactly follows this understanding.*

RESCALE and RESHIFT. Our investigation is based on the above understanding. As introduced in Sec. 2.2, there are three standard re-normalization approaches: RESET for models with BatchNorm, implicit normalization in models with LayerNorm, and REPAIR for general architectures. One challenge to universally understanding re-normalization is that the BatchNorm and LayerNorm are poorly understood as well. To make the problem more addressable, our primary emphasis in this section is on REPAIR and plain models. In REPAIR, an affine transformation is applied to each selected channel to correct the statistics. It’s natural to ask *whether the re-scaling and re-shift are equivalently important to the success of REPAIR*. Notably, although a single re-shift did not explicitly recover the activation variance, its correction effect might still improve the model (see Appendix G.1). For a detailed comparison, we designed two variants of REPAIR:

$$\text{RESCALE: } \tilde{N}_\lambda^{(i,j)}(x) \leftarrow \frac{\tilde{N}_\lambda^{(i,j)}(x)}{\sigma_\lambda^{(i,j)}} \cdot w_\lambda^{(i,j)}, \text{ RESHIFT: } \tilde{N}_\lambda^{(i,j)}(x) \leftarrow \tilde{N}_\lambda^{(i,j)}(x) - \mu_\lambda^{(i,j)} + b_\lambda^{(i,j)}, \quad (2)$$

where the same notions are adopted as (1). We assessed the performance of each method in repairing the post-matching midpoint model between two independently trained plain models. VGG16, plain ResNet20, and Fixup ResNet20 results on CIFAR-10 are shown in Table 1. Interestingly, it was observed that a single RESCALE improved the merged model to a similar extent as REPAIR,

Table 2: Investigation of activation statistics correction. Average activation statistics in the 5-th convolutional layer are reported. The end models are two independently trained VGG16 on CIFAR-10. No re-normalization is utilized for columns “-”. The reference statistics, i.e., statistics of the end models are in bold. It’s expected that re-normalization can recover statistics of the midpoint model to be similar to the ones of end models.

Average Statistics	End Model		Post-Matching Midpoint Model			Midpoint Model		
	1	2	-	REPAIR	RESCALE	-	REPAIR	RESCALE
Pre-Activation Scale	55.30	66.03	12.94	59.82	65.35	0.55	54.00	75.93
Post-Activation Scale	2.33	2.38	0.23	2.17	1.21	0.00	0.48	0.17
Pre-Activation Std.	42.83	48.88	8.93	45.58	45.49	0.30	37.87	43.26
Post-Activation Std.	7.54	7.96	0.87	6.96	4.55	0.00	1.92	0.88
Zero Post-Activation	89.7%	90.87%	94.19%	-	-	98.8%	-	-

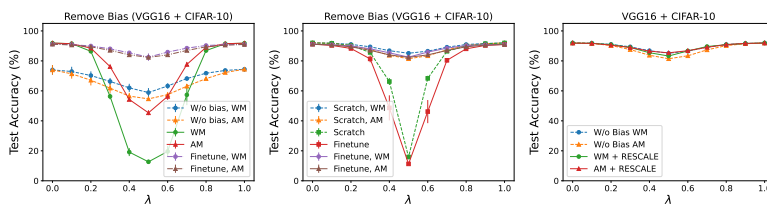


Figure 2: Removing biases from the model can benefit model re-basin. **(A)** After removing biases from end models, the post-matching barrier between them suddenly shrinks. The small barrier remains even after fine-tuning the two end models. **(B)** Removing biases from end models at initialization (“Scratch”) or after training followed by fine-tuning (“Finetune”) decreases the barrier to the same extent. **(C)** Removing biases from models reduces the barrier to the same extent as applying RESCALE to models with biases.

while RESHIFT completely ruined the model. For VGG16, RESCALE even reduced the barrier by an additional 9% on average compared with REPAIR. Moreover, we found that RESCALE had comparable performances to REPAIR even when only the average std $\bar{w}_\lambda^{(i)} = \text{mean}_j(w_\lambda^{(i,j)})$ in each layer was provided. Besides the accuracy, we also investigated each method’s ability to correct activation statistics. Specifically, we calculated the average scale and standard deviation of pre-activation and post-activation in each layer of the end models and the post-matching midpoint model after re-normalization. We report the results of the VGG16 experiment in the first four rows of Table 2. The results suggest that RESCALE successfully recovered activation statistics of the post-matching midpoint model to a similar extent as REPAIR for both the pre-activation and post-activation. This correction effect was applied to all the layers in the midpoint model, mitigating the variance collapse. Indeed, scaling up the positive activation can also scale up the variance of the activation. Other results in Table 2 will be discussed in Sec. 4.1.

We provide results on more model architectures and datasets and the complete visualization of the above experiments in Appendix G.1. *In summary, our ablation study suggests that rescaling up the activation plays the main role in REPAIR.*

3.2 Insight: Sensitivity to Activation Shift

While the last subsection focuses on rescaling in re-normalization, there is another perspective to interpret these results. Table 1 and 2 indeed suggest that the *activation shift* is an unstable factor in REPAIR that completely removing it sometimes even helps. In our exploration, we noticed that this instability by activation shift seems to be a common characteristic in current re-basin practices.

Removing the Shift in Re-Normalization. Besides results presented in Sec. 3.1, we noticed that RESCALE is more robust than REPAIR when the end models are trained with less strong weight decay. Detailed discussions are provided in Sec. 4.2.

Removing the Shift in Model Biases. During our investigation, we noticed that, indeed, there is a natural activation shift that is brought by the biases in each layer of the model. Hence, it would be interesting to verify whether the performance of the model re-basin is also sensitive to this type of shift. As the first step, we continued to study the plain models and to consider removing the

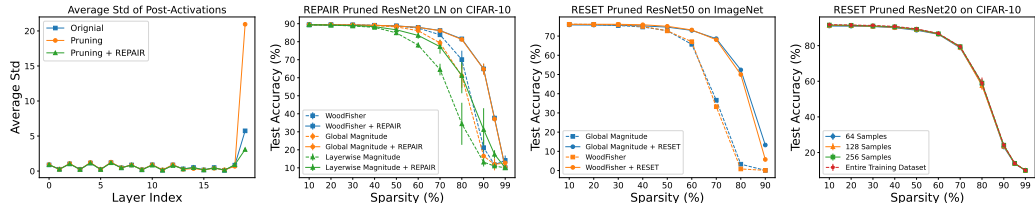


Figure 3: (A) Irregularity in the pruned model’s activation statistics. (B) & (C) Performance of REPAIR and RESET in improving the mode performance after pruning. (D) Using a single batch of data to estimate activation statistics is often sufficient to ensure effective re-normalization.

shift by removing the model biases. Two strategies were explored: removing the biases in two end models after training or at initialization. We discuss the results of VGG16 on CIFAR-10 below. As shown in Figure 2 (A), the post-WM midpoint model between two independent solutions initially performed as a random guess. However, by removing the biases in each layer from two end models, the new post-WM midpoint model significantly improved, albeit the end model worsened. We then considered fine-tuning the end models to recover training accuracy above 90%. It turned out that either applying the same permutation obtained before fine-tuning or applying a new matching at this time maintained the small barrier. Meanwhile, Figure 2 (B) shows that the same reduction in barrier can be obtained by training two end models without biases from scratch. On average, removing the biases in both scenarios significantly decreased the post-WM barrier from 79.19% to 8.54% and the post-AM barrier from 46.49% to 8.71%. Similar observations were drawn across other model architectures and datasets, see Appendix G.2. These results suggest that the activation shift brought by model biases could also greatly affect the re-basin performance. More interestingly, we noticed that removing biases from models reduced the barrier to the same extent as applying RESCALE, shown in Figure 2 (C). This observation connects the removal of activation shift from the two aspects.

Understanding this sensitivity could be a direction of great value, e.g., better handling of the activation shift might improve re-basin practice. While a more dedicated analysis of this complicated problem is beyond the scope of this work, we reveal an interesting connection below, which might provide more insights. In [56], the authors considered the linear interpolation between a random initialization and the SGD solution and revealed that the landscape shape along this line depends heavily on the model biases. Inspired by the theoretical analysis, they proposed the *homogenous interpolation* that can change the interpolation shape, but the barrier remained the same in their experiments. In Appendix G.3, we reported that the homogenous interpolation, surprisingly, can decrease the barrier in our setting to a similar extent as the two activation shift removal strategies described above. This similarity may allow one to utilize theoretical tools established in [56] to study the sensitivity.

In conclusion, our results suggest that re-basin performance is sensitive to the activation shift in the model, which can be influenced by re-normalization and bias terms in the model architecture. In some cases, completely removing the shift can even be beneficial. Exploring more nuanced approaches to handling the activation shifts could be a promising direction for future research. Understanding this sensitivity may also provide deeper insights into re-basin and linear mode connectivity.

3.3 A Novel Post-Pruning Plug-In

Previous studies have connected linear mode connectivity to the lottery ticket hypothesis [16, 19, 46]. This section provides a novel perspective to unify the re-basin and general pruning practices, which motivates us to derive a lightweight yet effective post-pruning plug-in.

At a high level, we found that pruning and re-basin can both be seen as processes that, given one or two SGD solutions, apply an algorithm to identify model parameters with specific properties, perform an arithmetic operation on model parameters accordingly, and finally produce a new model that is expected to have similar performance to the original. From this perspective, the pruned model resembles the merged model. Similar to the finding of variance collapse, we also discovered irregularities in the model activation after pruning. As shown in Figure 3 (A), after pruning 90% parameters of a ResNet20 LN trained on CIFAR-10 by one-shot global magnitude pruning, the standard deviation of the model output oddly increased by three times. Motivated by mitigating variance collapse in the merged model by re-normalization, we noticed that applying re-normalization

to the pruned model using the unpruned statistics can also alleviate the above-mentioned irregularities and improve the model accuracy, e.g., the accuracy increased by over 40% in Figure 3 (B).

These findings inspired us to apply re-normalization as a post-pruning technique to enhance the model performance. We examined three one-shot pruning approaches in experiments: global/layerwise magnitude pruning [24], diagonal-Fisher pruning, and the more complex WoodFisher pruning [50]. Appendix G.5 gives the details and complete results. To avoid interference, we adopted simple pruner hyperparameters without tuning, which is the reason for the non-optimal performance of WoodFisher. Across all models and datasets considered, RESET (Figure 3 (C)) and REPAIR significantly improved the performance of pruned models, especially at a higher sparsity. Moreover, this technique is very cost-effective: (1) no additional parameters are added to the model, and (2) it requires minimal data (often one batch, see Figure 3 (D)) to estimate the activation statistics. This is particularly advantageous in resource-constrained environments like federated learning [42] on end devices. Besides, its post-pruning feature makes integrating with any existing pruning framework simple. Exploring the performance of this technique in more general settings is a promising future direction.

4 Rethinking Matching

Although the importance of re-normalization has been emphasized multiple times in previous sections, empirical evidence from prior studies suggested the most indispensable component in current re-basin practices is the matching. A single weight matching or activation matching can achieve the linear mode connectivity in simple settings while applying re-normalization brings no improvement without matching [3, 32]. However, current understanding and development around matching is even more limited than re-normalization. One of the reasons is that this task is highly intricate, e.g. weight matching is known to be an NP-hard problem [3]. To gain meaningful insights, we were inspired by the research process of REPAIR as described in [32]. The approach involves first identifying an irregular phenomenon in the merged model and then proposing a method to mitigate this irregularity. Ideally, this method would not only alleviate the irregularity but also reduce the barrier. If the barrier remains unchanged, understanding the underlying reasons can still provide valuable insights.

In the following sections, we report two novel irregularities observed in the merged model: *activation collapse* and *magnitude collapse*. By analyzing and alleviating these issues, we identified the positive impact of training end models with larger learning rates and stronger weight decay. Additionally, these findings explain failed attempts in previous works and unveil the impact of initialization strategies.

4.1 Activation Collapse

As stated earlier, Jordan et al. [32] observed that re-normalization without matching did not improve the merged model’s accuracy. To investigate the reason, we examined the activation statistics of the merged model, one of which is reported in the last six columns of Table 2. Notably, while the pre-ReLU activation statistics of the midpoint model were similarly restored by REPAIR or RESCALE regardless of matching, there was negligible improvement in post-ReLU activation statistics without matching. After careful examination, we identified one of the sources of this issue, as recorded in the last row of Table 2. We found that without matching, the midpoint model had, on average, 80% of its previously activated neurons become inactive (i.e., activations turned from positive to zero) when processing a sample, compared to the end model. We refer to this phenomenon as *activation collapse*. For RESCALE, activation collapse significantly reduces the number of post-activations that can be effectively scaled up, since $\text{ReLU}(x) = 0$ for all negative x . Given that rescaling plays a central role in REPAIR, as shown in Sec. 3.1, REPAIR likely also suffers from this issue. On the other hand, applying the matching reduced activation collapse by half in this case, thereby creating more space for effective rescaling and eventually decreasing the barrier. From here, an appealing question is: *can alleviating this issue in other ways also reduce the barrier?*

As the first step, we analyze a simple scenario in this paper. Assuming the first $i - 1$ layers of the two end models N_0, N_1 are perfectly aligned, i.e., $N_0^{(k)}(x) \approx N_1^{(k)}(x)$, for all x and $1 \leq k \leq i - 1$. Then the pre-activation of the i -th layer in the midpoint model is approximately the average of the pre-activation from the end models by linearity, i.e., $\tilde{N}_{1/2}^{(i)}(x) \approx (\tilde{N}_0^{(i)}(x) + \tilde{N}_1^{(i)}(x))/2$. Therefore, the activation collapse can only be caused by the positive pre-activation of one end model being mistakenly aligned with the negative pre-activation from the other. This does not seem to be an issue after matching, especially when activation matching is applied to seek the nearest activation vector. However, experimental results such as Table 2 suggest that the current activation matching algorithm

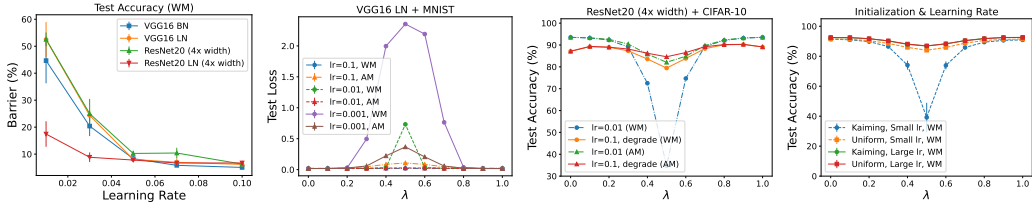


Figure 4: **(A)** Post-matching barriers decrease when end models are trained with a larger learning rate. **(B)** The usage of a too-small learning rate causes the substantial post-matching barrier reported in [3] between VGG16 LNs trained on MNIST. **(C)** Ablation study on the learning rate, suggesting that the barrier reduction is not solely due to higher test accuracy from larger learning rates. **(D)** Sensitivity to initialization strategy when using with a small learning rate. Learning rate is 0.1 and 0.01 in the plot.

still returns a large portion of such *severe mismatches* ($> 30\%$ in VGG experiments). From this perspective, avoiding such severe mismatches could be one way to mitigate the activation collapse.

Learning Rate. We take one unique perspective to interpret the performance of activation matching mentioned above. We hypothesize that this poor performance is partially due to the Euclidean distance used by the algorithm becoming less meaningful in higher-dimensional spaces [2, 9]. In Table 2, even when 90% of the components of the activation vector are zeros, the vector used in matching still has approximately $1638 \cdot B$ dimensions, where the batch size B is 128 in this experiment. Such high dimensionality challenges the matching process and potentially causes severe mismatches. Therefore, we expect the issue to be alleviated if the end models have sparser intermediate activations. We verified this idea, inspired by recent results suggesting that large learning rates can endow feature sparsity to the model [5]. Our experiments showed a reduction in activation collapse in some layers when end models were trained with larger learning rates (see Appendix H.1). More importantly, the post-matching barrier was also reduced, as shown in Figure 4 (A). Notably, increasing the learning rate from 0.01 to 0.1 reduced the barrier by more than 40% for VGG16 LN and ResNet20. Moreover, we noticed that this finding also explains a failed attempt in [3], where authors reported unsatisfactory results when matching VGG16 LNs trained on MNIST. Indeed, the large barrier can be attributed to the learning rate adopted in the experiment being too small. A zero barrier was achieved immediately after increasing the learning rate, as illustrated in Figure 4 (B). *In summary, these results suggest that current re-basin practices perform better between solutions obtained using larger learning rates.*

Although our discussions on activation collapse and feature sparsity led to the findings around learning rates, the underlying reason for this improvement might differ, as we did not provide rigorous theoretical support. While a theoretical understanding is beyond the scope of this work, we offer an empirical analysis of an alternative explanation below. Extensive previous research has shown that large learning rates can enhance the generalizability of solutions. Therefore, it is possible that the barrier reduction is trivially from the overall improved test accuracy. Yet, we observe two pieces of negative evidence against this view. Firstly, we observed that the barrier of training accuracy also reduced similarly. Note that the two end models always achieved nearly 100% training accuracy, even with lower learning rates, so the aforementioned explanation cannot account for this observation. Secondly, we conducted an ablation study where we retrained the solutions obtained by large learning rates until their test accuracy fell below that of solutions trained with a smaller learning rate. Figure 4 (C) shows that the post-matching barrier between models trained with a larger learning rate remained significantly lower, contradicting the previous hypothesis.

Initialization Strategy. During our study of learning rates, we noticed that initialization strategies can also impact re-basin effectiveness. We examined two standard initializations: Kaiming (normal) initialization and (Kaiming) uniform initialization [25]. As shown in Figure 4, while both strategies resulted in solutions with similar performance, the post-matching barrier was much larger between solutions with Kaiming initialization than those initialized uniformly. This difference disappeared when a larger learning rate was used. This phenomenon was observed in both VGG16 LN and ResNet20 LN models trained on CIFAR-10. In appendix H.1, we provide an analysis from the perspectives of initialization variance and model distance during training.

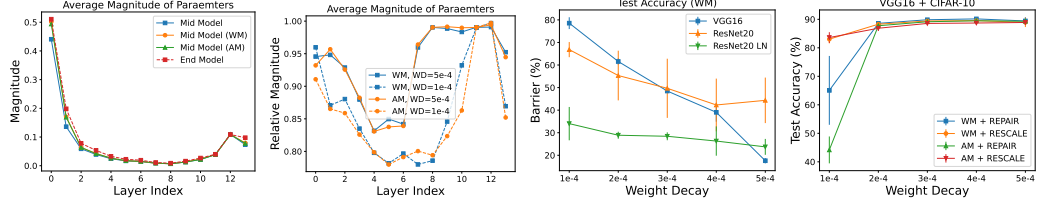


Figure 5: **(A)** Visualization of magnitude collapse in the midpoint model. **(B)** Stronger weight decay increases the relative magnitude of the merged model. **(C)** Post-matching barriers reduce when end models are trained with stronger weight decay. **(D)** RESCALE is more robust than REPAIR with weak weight decay. Test accuracy of the normalized post-matching midpoint model is reported.

4.2 Magnitude Collapse

Prior sections of the paper primarily focused on irregularities in the merged model’s activation. Indeed, we also observed issues in the parameters of the model. When aligning the parameters of a certain layer in two end models as pairs $\{(x_i, y_i)\}_{i=1}^n$, the corresponding parameters in the midpoint model are $\{(x_i + y_i)/2\}_{i=1}^n$. As shown in Figure 5 (A), the average parameter magnitude of several layers in the midpoint model noticeably decreased compared to the end models. We refer to this phenomenon as *magnitude collapse*. This issue was somewhat alleviated after applying matching. Since the reduction in average magnitude is proportional to $\sum_{i=1}^n (|x_i| + |y_i| - |x_i + y_i|)$, the issue indeed indicates that many parameters with opposite signs were incorrectly aligned.

Weight Decay. To mitigate the magnitude collapse, we considered a simple scenario where each x_i, y_i is independently drawn from the uniform distribution $U(\mu - \sigma, \mu + \sigma)$ ($\sigma, \mu > 0$). Clearly, the magnitude collapse occurs only when $\sigma > \mu$. In this case, we have $\mathbb{E}[|x_i| + |y_i| - |x_i + y_i|] = (\sigma + 2\mu)(\sigma - \mu)^2/3\sigma^2$, indicating that the degree of magnitude reduction diminishes as the variance σ shrinks, with a fixed μ . Inspired by this insight, we hypothesized that the magnitude collapse could be alleviated once limiting the parameters within a smaller region to bound the error. To ensure a fair comparison, we compared the relative magnitude in the post-matching midpoint model (i.e., divided by the magnitude of the end models’ parameters), as the absolute magnitude changes with weight decay. As shown in Figure 5 (B), stronger weight decay considerably recovered the relative magnitude across most layers, including the output layer. Moreover, the post-matching barrier also decreased with stronger weight decay (Figure 5 (C)). Notably, the post-WM barrier for VGG16 decreased by over 60% when the weight decay factor increased from $1e-4$ to $5e-4$. Similar to our learning rate analysis, ablation experiments and results around training accuracy suggest that the improved re-basin performance is not solely due to better generalization by stronger weight decay (see Appendix H.2). Further understanding of this phenomenon is an interesting direction for future research. We also provide a theoretical view below, elaborated in Appendix H.2. For the approximately low dimensional scenario in [15, Sec. 5.4], we noticed that constraining the parameter magnitude by decreasing the variance of the multivariate Gaussian μ_ℓ can provide a more accurate estimation $k_{\ell-1}$ of the intrinsic dimension $\tilde{m}_{\ell-1}$, lowering the upper bound over barrier given in [15, Theorem 5.4].

Additionally, we observed that weight decay also influences the effectiveness of re-normalization. As shown in Figure 5 (D), the improvements by REPAIR were unstable with smaller weight decay, but this issue diminished with stronger weight decay. On the other hand, RESCALE appeared more robust, performing well across different weight decay strengths. This supports our discussions in Sec. 3.2 that sometimes removing activation shifts can aid re-basin.

5 Conclusion

This paper provides several novel insights into model re-basin practices and linear mode connectivity. The empirical investigations unveil that rescaling is crucial in the REPAIR technique, while the re-basin performance is sensitive to the activation shifts in the model. This underscores the need for more nuanced approaches to managing the activation shifts to improve the re-basin practice. Meanwhile, the paper identifies the issues of activation collapse and magnitude collapse in merged models. The impact of the learning rates, weight decay, and initialization strategies is studied from there. Furthermore, a novel perspective that unifies model re-basin and pruning practices is proposed,

leading to a lightweight and effective post-pruning technique. These findings open new avenues in understanding the underlying principle and deriving better re-basin practices.

References

- [1] L. Adilova, A. Fischer, and M. Jaggi. Layerwise linear mode connectivity. *arXiv preprint arXiv:2307.06966*, 2023.
- [2] C. C. Aggarwal, A. Hinneburg, and D. A. Keim. On the surprising behavior of distance metrics in high dimensional space. In *Database Theory—ICDT 2001: 8th International Conference London, UK, January 4–6, 2001 Proceedings 8*, pages 420–434. Springer, 2001.
- [3] S. K. Ainsworth, J. Hayase, and S. Srinivasa. Git re-basin: Merging models modulo permutation symmetries. *arXiv preprint arXiv:2209.04836*, 2022.
- [4] M. Andriushchenko, F. Croce, M. Müller, M. Hein, and N. Flammarion. A modern look at the relationship between sharpness and generalization. *arXiv preprint arXiv:2302.07011*, 2023.
- [5] M. Andriushchenko, A. V. Varre, L. Pillaud-Vivien, and N. Flammarion. Sgd with large step sizes learns sparse features. In *International Conference on Machine Learning*, pages 903–925. PMLR, 2023.
- [6] J. L. Ba, J. R. Kiros, and G. E. Hinton. Layer normalization. *arXiv preprint arXiv:1607.06450*, 2016.
- [7] G. Benton, W. Maddox, S. Lotfi, and A. G. G. Wilson. Loss surface simplexes for mode connecting volumes and fast ensembling. In *International Conference on Machine Learning*, pages 769–779. PMLR, 2021.
- [8] F. Benzing, S. Schug, R. Meier, J. Von Oswald, Y. Akram, N. Zucchetti, L. Aitchison, and A. Steger. Random initialisations performing above chance and how to find them. *arXiv preprint arXiv:2209.07509*, 2022.
- [9] K. Beyer, J. Goldstein, R. Ramakrishnan, and U. Shaft. When is “nearest neighbor” meaningful? In *Database Theory—ICDT’99: 7th International Conference Jerusalem, Israel, January 10–12, 1999 Proceedings 7*, pages 217–235. Springer, 1999.
- [10] L. Chizat and F. Bach. On the global convergence of gradient descent for over-parameterized models using optimal transport. *Advances in neural information processing systems*, 31, 2018.
- [11] J. Deng, W. Dong, R. Socher, L.-J. Li, K. Li, and L. Fei-Fei. Imagenet: A large-scale hierarchical image database. In *2009 IEEE conference on computer vision and pattern recognition*, pages 248–255. Ieee, 2009.
- [12] L. Dinh, R. Pascanu, S. Bengio, and Y. Bengio. Sharp minima can generalize for deep nets. In *International Conference on Machine Learning*, pages 1019–1028. PMLR, 2017.
- [13] F. Draxler, K. Veschgini, M. Salmhofer, and F. Hamprecht. Essentially no barriers in neural network energy landscape. In *International conference on machine learning*, pages 1309–1318. PMLR, 2018.
- [14] R. Entezari, H. Sedghi, O. Saukh, and B. Neyshabur. The role of permutation invariance in linear mode connectivity of neural networks. *arXiv preprint arXiv:2110.06296*, 2021.
- [15] D. Ferbach, B. Goujaud, G. Gidel, and A. Dieuleveut. Proving linear mode connectivity of neural networks via optimal transport. *arXiv preprint arXiv:2310.19103*, 2023.
- [16] S. Fort, G. K. Dziugaite, M. Paul, S. Kharaghani, D. M. Roy, and S. Ganguli. Deep learning versus kernel learning: an empirical study of loss landscape geometry and the time evolution of the neural tangent kernel. *Advances in Neural Information Processing Systems*, 33:5850–5861, 2020.
- [17] J. Frankle. Revisiting" qualitatively characterizing neural network optimization problems". *arXiv preprint arXiv:2012.06898*, 2020.
- [18] J. Frankle and M. Carbin. The lottery ticket hypothesis: Finding sparse, trainable neural networks. *arXiv preprint arXiv:1803.03635*, 2018.
- [19] J. Frankle, G. K. Dziugaite, D. Roy, and M. Carbin. Linear mode connectivity and the lottery ticket hypothesis. In *International Conference on Machine Learning*, pages 3259–3269. PMLR, 2020.

[20] C. D. Freeman and J. Bruna. Topology and geometry of half-rectified network optimization. *arXiv preprint arXiv:1611.01540*, 2016.

[21] T. Garipov, P. Izmailov, D. Podoprikhin, D. P. Vetrov, and A. G. Wilson. Loss surfaces, mode connectivity, and fast ensembling of dnns. *Advances in neural information processing systems*, 31, 2018.

[22] I. J. Goodfellow, O. Vinyals, and A. M. Saxe. Qualitatively characterizing neural network optimization problems. *arXiv preprint arXiv:1412.6544*, 2014.

[23] A. Gotmare, N. S. Keskar, C. Xiong, and R. Socher. Using mode connectivity for loss landscape analysis. *arXiv preprint arXiv:1806.06977*, 2018.

[24] S. Han, J. Pool, J. Tran, and W. Dally. Learning both weights and connections for efficient neural network. *Advances in neural information processing systems*, 28, 2015.

[25] K. He, X. Zhang, S. Ren, and J. Sun. Delving deep into rectifiers: Surpassing human-level performance on imagenet classification. In *Proceedings of the IEEE international conference on computer vision*, pages 1026–1034, 2015.

[26] K. He, X. Zhang, S. Ren, and J. Sun. Deep residual learning for image recognition. In *Proceedings of the IEEE conference on computer vision and pattern recognition*, pages 770–778, 2016.

[27] R. Hecht-Nielsen. On the algebraic structure of feedforward network weight spaces. In *Advanced Neural Computers*, pages 129–135. Elsevier, 1990.

[28] G. Ilharco, M. T. Ribeiro, M. Wortsman, S. Gururangan, L. Schmidt, H. Hajishirzi, and A. Farhadi. Editing models with task arithmetic. *arXiv preprint arXiv:2212.04089*, 2022.

[29] M. Imfeld, J. Graldi, M. Giordano, T. Hofmann, S. Anagnostidis, and S. P. Singh. Transformer fusion with optimal transport. *arXiv preprint arXiv:2310.05719*, 2023.

[30] S. Ioffe and C. Szegedy. Batch normalization: Accelerating deep network training by reducing internal covariate shift. In *International conference on machine learning*, pages 448–456. pmlr, 2015.

[31] P. Izmailov, D. Podoprikhin, T. Garipov, D. Vetrov, and A. G. Wilson. Averaging weights leads to wider optima and better generalization. *arXiv preprint arXiv:1803.05407*, 2018.

[32] K. Jordan, H. Sedghi, O. Saukh, R. Entezari, and B. Neyshabur. Repair: Renormalizing permuted activations for interpolation repair. *arXiv preprint arXiv:2211.08403*, 2022.

[33] J. Juneja, R. Bansal, K. Cho, J. Sedoc, and N. Saphra. Linear connectivity reveals generalization strategies. *arXiv preprint arXiv:2205.12411*, 2022.

[34] N. S. Keskar, D. Mudigere, J. Nocedal, M. Smelyanskiy, and P. T. P. Tang. On large-batch training for deep learning: Generalization gap and sharp minima. *arXiv preprint arXiv:1609.04836*, 2016.

[35] A. Krizhevsky, G. Hinton, et al. Learning multiple layers of features from tiny images. 2009.

[36] J. Kwon, J. Kim, H. Park, and I. K. Choi. Asam: Adaptive sharpness-aware minimization for scale-invariant learning of deep neural networks. In *International Conference on Machine Learning*, pages 5905–5914. PMLR, 2021.

[37] Y. LeCun, L. Bottou, Y. Bengio, and P. Haffner. Gradient-based learning applied to document recognition. *Proceedings of the IEEE*, 86(11):2278–2324, 1998.

[38] B. Li, B. Wu, J. Su, and G. Wang. Eagleeye: Fast sub-net evaluation for efficient neural network pruning. In *Computer Vision–ECCV 2020: 16th European Conference, Glasgow, UK, August 23–28, 2020, Proceedings, Part II 16*, pages 639–654. Springer, 2020.

[39] Z. Liu, H. Mao, C.-Y. Wu, C. Feichtenhofer, T. Darrell, and S. Xie. A convnet for the 2020s. In *Proceedings of the IEEE/CVF conference on computer vision and pattern recognition*, pages 11976–11986, 2022.

[40] E. S. Lubana, E. J. Bigelow, R. P. Dick, D. Krueger, and H. Tanaka. Mechanistic mode connectivity. In *International Conference on Machine Learning*, pages 22965–23004. PMLR, 2023.

[41] S. Marcel and Y. Rodriguez. Torchvision the machine-vision package of torch. In *Proceedings of the 18th ACM international conference on Multimedia*, pages 1485–1488, 2010.

[42] B. McMahan, E. Moore, D. Ramage, S. Hampson, and B. A. y Arcas. Communication-efficient learning of deep networks from decentralized data. In *Artificial intelligence and statistics*, pages 1273–1282. PMLR, 2017.

[43] V. Nagarajan and J. Z. Kolter. Uniform convergence may be unable to explain generalization in deep learning. *Advances in Neural Information Processing Systems*, 32, 2019.

[44] B. Neyshabur, H. Sedghi, and C. Zhang. What is being transferred in transfer learning? *Advances in neural information processing systems*, 33:512–523, 2020.

[45] A. Paszke, S. Gross, F. Massa, A. Lerer, J. Bradbury, G. Chanan, T. Killeen, Z. Lin, N. Gimelshein, L. Antiga, et al. Pytorch: An imperative style, high-performance deep learning library. *Advances in neural information processing systems*, 32, 2019.

[46] M. Paul, F. Chen, B. W. Larsen, J. Frankle, S. Ganguli, and G. K. Dziugaite. Unmasking the lottery ticket hypothesis: What’s encoded in a winning ticket’s mask? *arXiv preprint arXiv:2210.03044*, 2022.

[47] F. Pittorino, A. Ferraro, G. Perugini, C. Feinauer, C. Baldassi, and R. Zecchina. Deep networks on toroids: removing symmetries reveals the structure of flat regions in the landscape geometry. In *International Conference on Machine Learning*, pages 17759–17781. PMLR, 2022.

[48] A. Rame, M. Kirchmeyer, T. Rahier, A. Rakotomamonjy, P. Gallinari, and M. Cord. Diverse weight averaging for out-of-distribution generalization. *Advances in Neural Information Processing Systems*, 35:10821–10836, 2022.

[49] K. Simonyan and A. Zisserman. Very deep convolutional networks for large-scale image recognition. *arXiv preprint arXiv:1409.1556*, 2014.

[50] S. P. Singh and D. Alistarh. Woodfisher: Efficient second-order approximation for neural network compression. *Advances in Neural Information Processing Systems*, 33:18098–18109, 2020.

[51] S. P. Singh and M. Jaggi. Model fusion via optimal transport. *Advances in Neural Information Processing Systems*, 33:22045–22055, 2020.

[52] M. Sun, Z. Liu, A. Bair, and J. Z. Kolter. A simple and effective pruning approach for large language models. *arXiv preprint arXiv:2306.11695*, 2023.

[53] N. Tattro, P.-Y. Chen, P. Das, I. Melnyk, P. Sattigeri, and R. Lai. Optimizing mode connectivity via neuron alignment. *Advances in Neural Information Processing Systems*, 33:15300–15311, 2020.

[54] A. Vaswani, N. Shazeer, N. Parmar, J. Uszkoreit, L. Jones, A. N. Gomez, Ł. Kaiser, and I. Polosukhin. Attention is all you need. *Advances in neural information processing systems*, 30, 2017.

[55] H. Wang, M. Yurochkin, Y. Sun, D. Papailiopoulos, and Y. Khazaeni. Federated learning with matched averaging. *arXiv preprint arXiv:2002.06440*, 2020.

[56] X. Wang, A. N. Wang, M. Zhou, and R. Ge. Plateau in monotonic linear interpolation—a “biased” view of loss landscape for deep networks. *arXiv preprint arXiv:2210.01019*, 2022.

[57] M. Wortsman, M. C. Horton, C. Guestrin, A. Farhadi, and M. Rastegari. Learning neural network subspaces. In *International Conference on Machine Learning*, pages 11217–11227. PMLR, 2021.

[58] M. Wortsman, G. Ilharco, S. Y. Gadre, R. Roelofs, R. Gontijo-Lopes, A. S. Morcos, H. Namkoong, A. Farhadi, Y. Carmon, S. Kornblith, et al. Model soups: averaging weights of multiple fine-tuned models improves accuracy without increasing inference time. In *International Conference on Machine Learning*, pages 23965–23998. PMLR, 2022.

[59] M. Yamada, T. Yamashita, S. Yamaguchi, and D. Chijiwa. Revisiting permutation symmetry for merging models between different datasets. *arXiv preprint arXiv:2306.05641*, 2023.

[60] D. Yunis, K. K. Patel, P. H. P. Savarese, G. Vardi, J. Frankle, M. Walter, K. Livescu, and M. Maire. On convexity and linear mode connectivity in neural networks. In *OPT 2022: Optimization for Machine Learning (NeurIPS 2022 Workshop)*, 2022.

[61] H. Zhang, Y. N. Dauphin, and T. Ma. Fixup initialization: Residual learning without normalization. *arXiv preprint arXiv:1901.09321*, 2019.

- [62] Z. Zhou, Y. Yang, X. Yang, J. Yan, and W. Hu. Going beyond linear mode connectivity: The layerwise linear feature connectivity. *arXiv preprint arXiv:2307.08286*, 2023.
- [63] M. Zimmer, C. Spiegel, and S. Pokutta. Sparse model soups: A recipe for improved pruning via model averaging. *arXiv preprint arXiv:2306.16788*, 2023.

Appendix

The appendix includes complete results of experiments reported in the main paper and additional results and discussions that cannot be presented in the main body due to space limits. The organization is as follows:

Appendix A. Discuss the broader impact of this work.

Appendix B. Discuss the limitations of this work and some future work.

Appendix C. Provide additional related work.

Appendix D. Provide experimental details of this work.

Appendix F. Supplementary to Section 2, including the comparison of different implementations of activation matching in [3], [32], and this work.

Appendix G. Supplementary to Section 3, including additional plots/tables, discussion of the independent reference model, post-activation REPAIR, irregularity in loss in experiments around the activation shift, and two novel re-normalization variants.

Appendix H. Supplementary to Section 4, including additional plots, detailed experiment settings of the ablation experiments, analysis of the initialization strategy, and elaboration of the theoretical view about the weight decay.

A Broader Impact Statement

This paper presents work whose goal is to advance the field of Machine Learning. There are many potential societal consequences of our work, none of which we feel must be specifically highlighted here.

B Limitation and Future Work

- As one of the first in-depth studies towards understanding previous successes and failures in model re-basin, this work only focuses on the fundamental setup — re-basing models trained on the same dataset to remove unnecessary difficulties and concentrate on the intrinsic principle. Meanwhile, our exploration only considers the most studied model architectures and datasets in prior works to thoroughly revisit the standard practice. We leave the consideration of more networks (e.g., transformer-based models as studied in [29]) and datasets for future work.
- As the first step to understanding this complicated problem, results reported in this work are primarily by empirical exploration. Although extensive experimental results and simple theoretical analysis support our insights on activation shift, activation collapse, magnitude collapse, etc., a rigorous theoretical framework is lacking. We leave the dedicated theoretical understanding for future work.
- Although several strategies are proposed to verify the novel understandings in this paper, they cannot be directly used as general methods to improve re-basin performance. For instance, the improvement diminishes when the learning rate and weight decay are too large. However, we emphasize that these findings indeed connect these diverse directions. The revealed relationships suggest the possibility of leveraging previous understandings of learning rates and weight decay to explore re-basin and linear mode connectivity further. We leave this exploration for future work.
- With the main focus on model re-basin and the linear mode connectivity, we only demonstrate the power of re-normalization in pruning in the one-shot pruning scenario. Yet, we emphasize that the same logic applies to other pruning frameworks, e.g., structured pruning and gradual pruning. We regard this as a promising direction worthy of further exploration and leave this as our future work. This super lightweight yet powerful technique is especially believed to be valuable in resource-limited deep learning. Meanwhile, we only consider a simple hyperparameter setting for the advanced WoodFisher pruner, i.e., fisher subsample size = 80 and fisher mini-batch size = 100 for ImageNet pruning, to save computational

cost. Although this restricts the ability of the pruner, a significant improvement by REPAIR/RESET is already demonstrated in our results and should be universal after merely changing some hyperparameters. We leave the efforts towards improving the SOTA results for future work.

C More Related Work

Mode Connectivity. Early works [13, 21] conjectured and empirically verified that the different neural network loss minima could indeed be connected by simple curves along which the loss remains low — a phenomenon called *Mode Connectivity*. [20] provided an asymptotical proof on half-rectified single-layer networks. [23] empirically validated the claim in extreme cases where the input models were trained or initialized differently. [53] proposed a neuron alignment algorithm that seeks permutations between trained networks, after which it is easier to learn a simple, planar, low-loss curve efficiently. [57, 7] directly learned lines, curves, and simplexes, preserving the mode connectivity. Generally, the mode connectivity can also be used to analyze, e.g., the loss landscape [23] and the model’s mechanisms [40].

Linear Mode Connectivity. Regarding the linear case, the LMC was first observed to exist between solutions trained from the same initialization. The shared initialization can either be a checkpoint in early training [43, 19] or a pre-trained network served as the starting point in transfer learning [44]. Empirical observations [44, 16] suggested that these models were trained into the same basin on the loss landscape, and averaging them could produce a better-performed model and save the additional storage and computational cost compared to model ensemble [58, 63, 31, 33]. The latter improvement is reasonable, assuming the basin is nearly convex, and hence, the average model is closer to the center of the basin. One empirical support for this intuition was demonstrated in [60], where the authors found a high-dimensional convex hull of low loss between the endpoints of several SGD trajectories. The LMC was also found to have connections to a wide range of fields, including the Lottery Ticket Hypothesis [19, 18, 46] and the neural tangent kernel (NTK) [16]. In the context of transfer learning, [33] found that the fine-tuned models could be divided into distinct clusters where LMC only existed between models within the same cluster. Model averaging/merging is also found to be highly helpful on the large language models [28].

Model Re-Basin/Fusion. On the other hand, a substantial linear barrier was often observed [44, 19] between independent SGD solutions, which restricts the application of model averaging. [14] compared models trained from different initializations and conjectured that the barrier could be eliminated after accounting for the permutation invariance of neural networks, assuming the model is wide enough. The claim was proved for a wide enough fully connected network with a single hidden layer at initialization. Although the paper failed to empirically validate this conjecture by finding desired permutations to re-basin the model, a successful attempt was shown in [3], where three different matching algorithms were derived for this purpose. Notably, these algorithms succeeded in obtaining the zero-barrier LMC between independently trained ResNet models on CIFAR-10 for the first time. Prior and concurrent work in this direction includes [8] proposing a matching algorithm to align models at initialization and [51] deriving a powerful optimal-transport-based algorithm. The latter work focused on the soft alignment (a.k.a., model fusion) between models and is hence not particularly considered in our work. Recent work in this direction is [29] providing efforts to fuse transformers [54]. It’s also noteworthy that the matching algorithms proposed in many works have some common points, e.g., the activation matching algorithm in [3] and [51] and the matching algorithm in [53]. While a significant improvement was seen in [3], [32] emphasized that this success highly depended on the utilization of normalization layers in models, including BatchNorm (with RESET) and LayerNorm, and the matching algorithms performed poorly on plain models without normalization layers. The authors attributed this to the issue of “variance collapse” and addressed it by proposing REPAIR — an extension of RESET that could work on plain models. Despite the extensive empirical studies, the understanding of this field remains limited. A theoretical effort was recently provided in [15], which proved the LMC via model re-basin in the mean field regime and generalized the results to deep networks under some assumptions.

Besides the original re-basin practices between two models trained on the same dataset, [59, 3, 32] explored aligning models trained on different datasets, and a preliminary result on matching multiple MLPs trained on MNIST was reported in [3]. Recently, [1] and [62] studied the *Layerwise Linear Mode Connectivity*. [47] utilized the re-basin approaches to remove symmetry and revealed the

structure of flat regions in the loss landscape. Different from the standard re-basin practice, scaling invariance is also considered.

D Experimental Details

We present the experimental details in this section.

Training Setting. The fundamental training framework is based on the standard setup [19, 26]. We train the model with standard SGD (momentum = 0.9) with a batch size of 128. For standard training of VGG and ResNet on CIFAR-10 and CIFAR-100, the model is trained for 160 epochs with a step decay learning rate initialized at 0.1 and reduced by a factor of 10 at iteration 32,000 and 48,000 (\sim epoch 82 and 123). Weight decay is set as $wd = 10^{-4}$. For the learning rate comparison experiment in Section 4.1, the initial learning rate is selected from [0.01, 0.03, 0.05, 0.07, 0.1]. For the weight decay experiment in Section 4.2, the weight decay factor is selected from $[10^{-4}, 2 \times 10^{-4}, 3 \times 10^{-4}, 4 \times 10^{-4}, 5 \times 10^{-4}]$.

For smooth training, we modify the training settings of certain models. There are two different learning rate schedules for this. For training VGG16 with $wd > 10^{-4}$, VGG16 ($8 \times$ width), ResNet20 ($4 \times$ width), and ResNet20 LN, the learning rate linearly increases in the first epoch from 10^{-6} to 0.1 and then follows the same step decay schedule. For training VGG16 without biases, plain ResNet20/ResNet32 (with and without biases), and Fixup ResNet20, the learning rate experiences the same linear warm-up in the first epoch but then follows a cosine annealing schedule. For training VGG16 LN with Kaiming uniform initialization, both learning schedules work well, and most of the results (e.g., when comparing different initializations in Section 4.1) reported in the paper are based on the step decay schedule with a linear warm-up. The same linear warm-up + cosine annealing schedule is applied when training VGG11 on CIFAR-100, but the warm-up takes two epochs. In our experiments, we didn't observe differences brought by the learning rate schedule, and those modifications were just for robust training.

For training VGG16 LN on MNIST reported in Section 4.1, we replicated the training setting of [3]. The model is initialized with Kaiming uniform initialization and trained for 25 epochs with SGD (momentum = 0.9). The learning rate linearly increases within the first epoch until reaching the maximum 0.001/0.01/0.1 and then follows a cosine annealing schedule. The training batch size is 100. Weight decay is set as $wd = 5 \times 10^{-4}$.

Model Architecture. The basic architectures of VGG and ResNet for CIFAR-10 and CIFAR-100 follow [19] and are standard in relevant practices. We edit the normalization layers accordingly in the plain/BN/LN version. We also consider the one with biases in convolutional layers for plain ResNet. The code for Fixup ResNet is adapted from the original paper [61]. For pruning ResNet50 and ConvNeXt-T on ImageNet, we directly utilized the pre-trained network in Torchvision [41].

Dataset. For the MNIST and CIFAR-10/CIFAR-100 datasets, we use the data provided by Torchvision. For ImageNet, we use the official release from its website¹. We perform the standard preprocessing to each dataset.

- **MNIST:** Each image is centered normalized by.
- **CIFAR-10/CIFAR-100:** Each image is center normalized. For training data, a random cropping (size = 32×32 , padding = 4) and random horizontal flipping are applied to each image before the re-normalization.
- **ImageNet:** For test data, each image is first resized to 256×256 and then center-cropped to 224×224 . We didn't utilize the training data in our experiments since we directly adapted the pre-trained checkpoints provided by Torchvision

Compute Resources. All experiments reported in this paper ran on NVIDIA A100-40GB and NVIDIA RTX A5500-24GB GPUs.

E The “Basin” View

This subsection briefly introduces the conventional “basin” view in research around (linear) mode connectivity, model merging, model re-basin, etc. This is where the name “re-basin” comes from.

¹<https://www.image-net.org/download.php>

Standard deep learning trains a randomly initialized neural network through optimization algorithms like SGD to minimize the empirical loss, moving the model downward on the loss landscape and ultimately converging at a “basin”. Roughly speaking, the word “basin” refers to a low-loss region around a local minimum in the literature. Understanding the basin can provide insights into the properties of solutions located in this basin. The basin also conveys information about the loss landscape. Yet, a clearer and unified view of the basin hasn’t been proposed.

One of the most common understandings is that the basin is a near-convex region around a solution, which is explicitly or implicitly adopted in most literature on model merging [31, 63, 58]. Recent evidence supporting the convexity includes [60]. This simple definition intuitively explains the improved performance of the model merging: if multiple models are located around the edge of the near-convex basin, averaging them can create a model closer to the basin’s center, which is preferred, e.g., when some noises shift the landscape. In this sense, this understanding is intrinsically the same as that of the flatness of minima [34, 36].

However, the above understanding seems to be restrictive in many aspects. For instance, there is evidence in prior works showing that this understanding of flatness may not be the most accurate [12, 4]. On the other hand, the mode connectivity finding also suggests the existence of more general low-loss regions around a solution.

Re-Basin. [14] proposed this basin conjecture for the first time:

Conjecture E.1 (Informal, from [14]). *Most SGD solutions belong to a set \mathcal{S} whose elements can be permuted in such a way that there is no barrier on the linear interpolation between any two permuted elements in \mathcal{S} .*

The paper then interpreted this conjecture in the following way: most SGD solutions end up in the same basin in the loss landscape after proper permutation. Although a clear definition of the basin was not given in the paper, the near-convex understanding is utilized in many figures in this direction [14, 3]. Meanwhile, since model re-basin can be seen as the generalization of previous model merging attempts, it’s natural and reasonable to inherit this understanding. This conjecture and understanding is then utilized in later literature in this direction. In particular, [3] confirmed the conjecture in several cases and proposed the name “re-basin” to summarize their approaches.

F Supplementary to “Preliminaries”

The section supplements Section 2 in the main paper.

F.1 Practical Calculation of Barrier

In our experiments, it was observed that the maximal barrier was almost surely achieved at the middle (i.e., $\lambda = 0.5$), and hence we simply set $\lambda = 0.5$ (Definition 2.1) when measuring the barrier to save computational cost. This empirical measurement is also adopted in [14]. We uniformly select 11 interpolation points between the two end models for all the interpolation plots reported in the paper.

F.2 Different Implementations of Activation Matching

In this section, we report the drawbacks in the performance of previous activation matching implementations, found in our experiments. Addressing the issues, we provide an improved implementation with the base trade-off between performance and computational efficiency.

Table 3: Compare different implementations of activation matching. Running on NVIDIA RTX A5500 (24G). The best results in each line are in bold.

Model	Barrier (Test Accuracy)			Running Time		
	Ours	A	B	Ours	A	B
VGG16	37.52 \pm 5.76%	54.87 \pm 5.12%	37.53 \pm 5.78%	17.87 \pm 0.29 s	7.75 \pm 0.09 s	40.91 \pm 0.35 s
VGG16 BN	3.51 \pm 0.15%	4.33 \pm 0.29%	3.49 \pm 0.13%	17.97 \pm 0.28 s	8.84 \pm 0.11 s	45.14 \pm 0.38 s
VGG16 LN	6.9 \pm 0.8%	9.71 \pm 0.66%	-	20.14 \pm 0.37 s	11.48 \pm 0.15 s	-
ResNet20	29.49 \pm 3.76%	32.45 \pm 2.15%	-	5.66 \pm 0.03 s	5.41 s	-
ResNet20 LN	23.05 \pm 1.84%	24.58 \pm 3.26%	-	8.21 \pm 0.09 s	9.12 \pm 0.18 s	-

We noticed that although [32] and [3] utilized the same activation matching algorithm, their implementations are different and the results can differ much. For convenience, we will refer to the implementation used in [3] as **A** and the one used in [32] as **B**. Both implementation **A** and **B** first estimate the activation statistics (mean and std.) of each layer in an online way and then solve the linear assignment problem based on the Pearson correlation calculated from the activation statistics. The main issue occurs in the former process, consisting of two parts: (1) implementation **A** utilizes the default `Float` data type, while **B** adopts a more accurate `Double` type; (2) to calculate the average covariance, implementation **A** first accumulates the summation by feeding the entire dataset to the model and then takes the average; while **B** calculates each batch average and then takes the average of batch averages. This results in a generally worse performance of implementation **A**.

Since this work aims to delve deeper into the SOTA practice and improve from there, we adopted the calculation strategy in **B**. We also noticed that although implementation **B** normally owned a better performance, it ran extremely slowly. The reason is that it performs the matching sequentially, i.e., re-feeding all the data to the model when matching each pair of layers; while **A** only feeds data in a single run and accumulates all the statistics simultaneously. In our experiments, we didn't find an obvious difference between them in performance. Therefore, our approach is mainly based on implementation **A** but utilizes the statistics accumulation strategy in **B**. We report the results on matching models trained on CIFAR-10 in Table 3. We compare the three implementations on plain VGG16 and VGG16 BN and compare our approach with implementation **A** in other settings. The results demonstrate that our approach has the best trade-off between high performance and computational efficiency.

G Supplementary to “Rethinking Re-Normalization”

The section supplements Section 3 in the main paper.

G.1 Deconstructing REPAIR

This subsection provides results and discussions in support of Section 3.1.

Complete Results. We provide the complete results of the ablation experiment on re-normalization below. The accuracy results are reported in Tables 4, 5, 6, and 7. We consider VGG16, plain ResNet20, and Fixup ResNet20 trained on CIFAR-10 and VGG11 trained on CIFAR-100. Both the weight matching and activation matching are examined. Test accuracy of the post-matching midpoint models before/after applying different re-normalization strategies is recorded in the tables, where end models are two independently trained models following the training framework in Appendix D. Across all the experiments, RESCALE consistently had comparable performances as REPAIR and outperformed REPAIR in the VGG16 + CIFAR-10 and VGG11 + CIFAR-100 experiments. In sharp contrast, the midpoint model performed as a random guess after a single RESHIFT.

Due to the space limit, the main paper only reports the activation statistics of the 5-th convolutional layers in the VGG experiment to support our analysis (Table 2). Here, we provide the complete visualizations of the activation statistics in the above-mentioned experiments in Figures 6, 7, 9 and 10. Activation statistics of each convolutional and linear layer in the end models and midpoint models are reported. Although the plots indeed convey more diverse information, we primarily focus on the similarity in the activation statistics between the midpoint model and end models. The matching algorithm and re-normalization strategies are expected to correct the activation statistics in the merged model, which is the midpoint model in these plots, to make it similar to the ones in the end models. From all these plots, we can clearly observe that a single RESCALE successfully restored the statistics to a similar extent as REPAIR, when matching was performed before that, supporting the crucial role of RESCALE in REPAIR. The comparison between results with or without re-normalization in the plots will be discussed in Appendix H.

In our experiments, we also noticed that the hidden activation statistics in the original midpoint model were similar to those in a randomly initialized model, shown in Figures 8 and 11. From the perspective of activation statistics, this highlights the need for certain techniques, such as matching and re-normalization, to correct the statistics and improve the model performance.

In summary, these results further support our claim that rescaling is the most important part of REPAIR.

Independent Reference Model. In our experiments, we drew an interesting observation: besides the end models, the reference model in RESCALE can even be selected as an independent solution. We report one result in Table 8. There, the independent RESCALE still significantly improves the interpolated model for both matching algorithms. Understanding this observation may provide novel insights into the re-normalization mechanism.

Sequential Re-Normalization. As discussed in the paper, the aim of REPAIR is to correct the statistics of hidden units in the interpolated network, including the activation mean and activation variance. Our experiments showed that a more accurate calculation in this process could further improve the performance. In the original implementation, after setting the goal statistics in the interpolated model, REPAIR simultaneously accumulates the activation statistics in each layer in a single run. However, the output of one layer is affected by early layers and hence a sequential calculation should return more accurate results. We verified this claim on VGG16 + CIFAR-10 with weight matching. As shown in Table 9, the sequential REPAIR outperforms the vanilla one by 8%, while no obvious differences were seen between RESCALE and sequential RESCALE. On the other hand, this finding also suggests that the complete failure of RESHIFT is not trivial, as more accurate activation means boosted by RESHIFT would also potentially improve the performance.

Post-Activation REPAIR. The standard REPAIR method corrects the activation statistics by modifying the pre-activation instead of the post-activation due to its better performance. Therefore, this paper also adopts the pre-activation REPAIR in experiments. We showcase such difference in performance in Table 10, where we compare the performance of pre-activation REPAIR and post-activation REPAIR in improving the midpoint model between two independent VGG16 solutions on CIFAR-10. Without matching, we noticed that neither the pre-activation REPAIR nor post-activation REPAIR improves the midpoint model. After weight matching, although post-activation REPAIR improves the midpoint model, the improvement is much less significant than pre-activation REPAIR.

Table 4: Ablation study on REPAIR, VGG16 + CIFAR-10. The first line records the test accuracy of the original post-activation-matching midpoint model. The best results in each column are in bold.

Variant	WM	AM
-	$14.22 \pm 2.27\%$	$48.68 \pm 7.22\%$
REPAIR	$75.1 \pm 4.09\%$	$43.71 \pm 3.36\%$
RESCALE	$84.32 \pm 0.77\%$	$83.72 \pm 2.03\%$
RESCALE (average)	$78.18 \pm 0.88\%$	$75.97 \pm 2.78\%$
RESHIFT	10%	10 %

Table 5: Ablation study on REPAIR, VGG11 + CIFAR-100. The first line records the test accuracy of the original post-matching midpoint model. The best results in each column are in bold.

Variant	WM	AM
-	$5.19 \pm 1.51\%$	$25.2 \pm 0.89\%$
REPAIR	$13.75 \pm 2.49\%$	$42.66 \pm 1.1\%$
RESCALE	$29.13 \pm 3.51\%$	$45.33 \pm 0.89\%$
RESCALE (average)	$18.19 \pm 2.44\%$	$34.06 \pm 0.86\%$
RESHIFT	1 %	$1 \pm 0.89\%$

Table 6: Ablation study on REPAIR, Plain ResNet20 + CIFAR-10. The first line records the test accuracy of the original post-matching midpoint model. The best results in each column are in bold.

Variant	WM	AM
-	$62.31 \pm 5.43\%$	$61.42 \pm 2.75\%$
REPAIR	$71.32 \pm 3.33\%$	$72.22 \pm 1.82\%$
RESCALE	$68.39 \pm 4.82\%$	$72.01 \pm 1.52\%$
RESCALE (average)	$61.05 \pm 6.51\%$	$65.81 \pm 3.18\%$
RESHIFT	$10.14 \pm 0.25\%$	$10.12 \pm 0.21\%$

Table 7: Ablation study on REPAIR, Fixup ResNet20 + CIFAR-10. The first line records the test accuracy of the original post-matching midpoint model. The best results in each column are in bold.

Variant	WM	AM
-	$38.84 \pm 1.89\%$	$42.81 \pm 0.23\%$
REPAIR	$63.62 \pm 2.73\%$	$73.32 \pm 0.15\%$
RESCALE	$61.85 \pm 3.43\%$	$71.42 \pm 0.23\%$
RESCALE (average)	$56.12 \pm 2.41\%$	$67.26 \pm 0.29\%$
RESHIFT	10 %	10 %

Table 8: Ablation study on RESCALE, VGG16 + CIFAR-10. Results with * utilize the reference activation statistics from an independent solution. The first line records the test accuracy of the original post-weight-matching midpoint model.

Variant	Test Accuracy
WM	10.49 %
WM + RESCALE*	68.89 %
WM + RESCALE (average)*	76.88 %
AM	43.98 %
AM + RESCALE*	68.64 %
AM + RESCALE (average)*	75.43 %

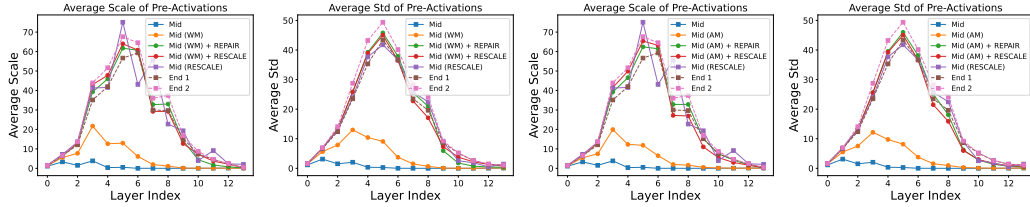


Figure 6: Pre-activation statistics of VGG16 trained on CIFAR-10, averaged in each layer.

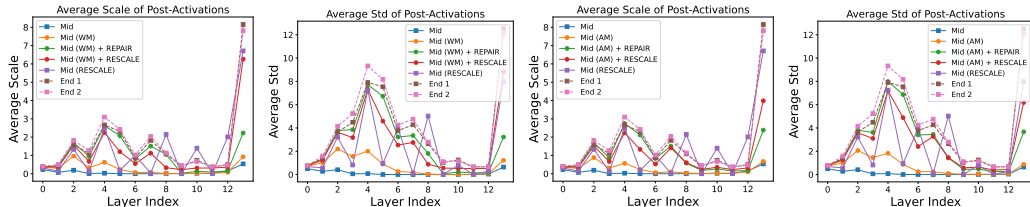


Figure 7: Post-activation statistics of VGG16 trained on CIFAR-10, averaged in each layer.

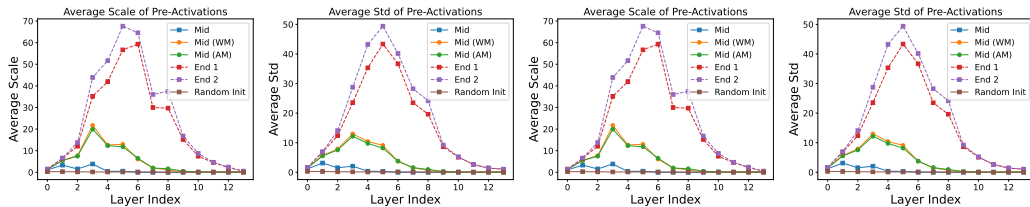


Figure 8: Pre-activation statistics of VGG16 trained on CIFAR-10, averaged in each layer. Compared with random initialization.

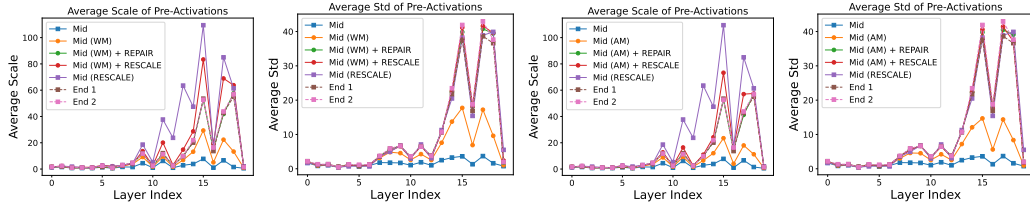


Figure 9: Pre-activation statistics of plain ResNet20 trained on CIFAR-10, averaged in each layer.

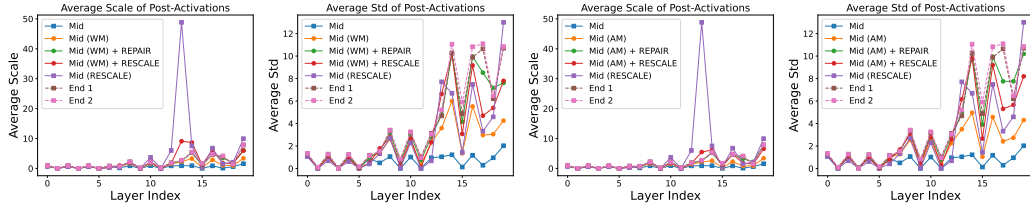


Figure 10: Post-activation statistics of plain ResNet20 trained on CIFAR-10, averaged in each layer.

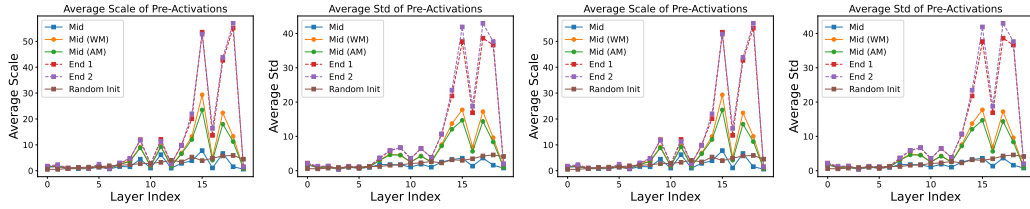


Figure 11: Pre-activation statistics of plain ResNet20 trained on CIFAR-10, averaged in each layer. Compared with random initialization.

Table 9: Compared with sequential re-normalization, evaluated on VGG16 + CIFAR-10. “SEQ” is short for “Sequential”. The best results in each column are in bold.

Variant	Train		Test	
	Acc	Loss	Acc	Loss
REPAIR	68.93%	1.59	65.75%	1.81
SEQ REPAIR	79.62%	1.33	75.38%	1.69
RESCALE	88.23%	0.59	83.63%	0.94
SEQ RESCALE	88.21%	0.59	83.57%	0.94

Table 10: Effect of applying pre-activation (“Pre-Act”) or post-activation (“Post-Act”) REPAIR to the midpoint model between two independently trained VGG16 on CIFAR-10. “W/o” means no re-normalization is applied. “W/o WM” means no matching algorithm is performed. The weight-matching is applied for results under “WM”. The best result is in bold.

	W/o WM			WM		
	W/o	Pre-Act.	Post-Act.	W/o	Pre-Act.	Post-Act.
Test Accuracy	10%	9.84%	10.42%	14.96%	76.95%	37.88%

G.2 Sensitivity to Activation Shift

Further results and discussions related to Section 3.2 are provided in this section. The finding around model biases is also motivated by the small barrier achieved on no-bias plain models in [51]. The connection between this finding and [56] is discussed in Appendix G.3.

Complete Results. We present the complete results of removing model biases at initialization or after training in Figures 12, 13, 14, 15, 16, 17, 18 and 19. The improvement in model accuracy brought by the removal of biases consistently holds among all the settings we considered, including VGG16/plain ResNet20 + CIFAR-10 and VGG11/plain ResNet20 + CIFAR-100. This supports that the re-basin performance is sensitive to the activation shift. Completely removing the shift can even improve the accuracy of the post-matching merged model.

Figure 20 and 21 visualize the similarity in performance between removing model biases and applying the re-normalization. Specifically, we compared it with RESCALE on VGG16 + CIFAR-10 and with REPAIR on plain ResNet20 + CIFAR-10, respectively. This interesting analogy could potentially provide more insights on how to improve the matching or post-matching process. For instance, one interesting question is what is the common issue alleviated by both strategies. If there is one such factor, it’s possible to improve the SOTA by directly optimizing it. We leave this for future work.

Irregularity in Loss. We also drew another interesting observation. We noticed that, although the post-matching linear barrier on the accuracy landscape significantly decreased after removing biases from the model, the barrier on the loss landscape remained, as shown in Figures 12, 13, 14, 15, 16, 17, 18 and 19. A similar observation was drawn by [56] where the homogeneous interpolation can only change the linear interpolation shape on the accuracy landscape. We regard this as one of the challenges for understanding why removing biases can improve performance and leave this for future work.

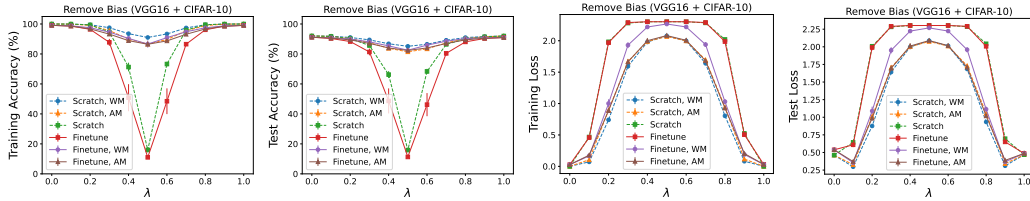


Figure 12: Training from scratch without biases vs. removing biases in a pre-trained model followed by fine-tuning. Linear interpolation between two VGG16 on CIFAR-10 is illustrated.

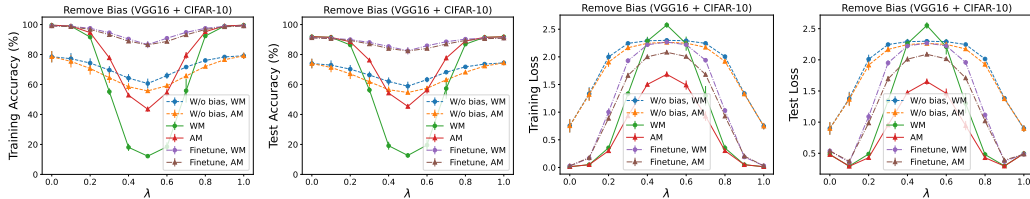


Figure 13: Removing biases in a pre-trained model followed by fine-tuning. Linear interpolation between two VGG16 on CIFAR-10 is illustrated.

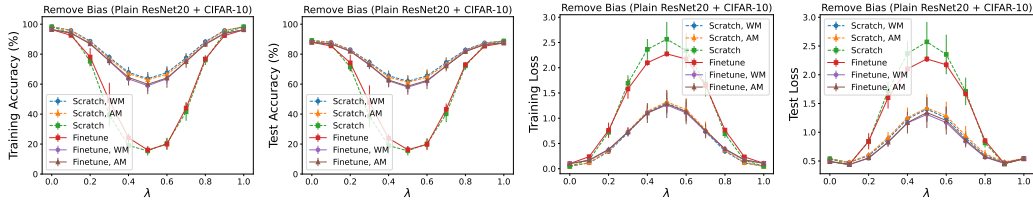


Figure 14: Training from scratch without biases vs. removing biases in a pre-trained model followed by fine-tuning. Linear interpolation between two plain ResNet20 on CIFAR-10 is illustrated.

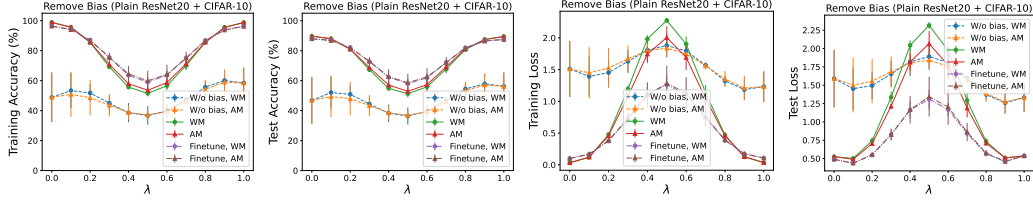


Figure 15: Removing biases in a pre-trained model followed by fine-tuning. Linear interpolation between two plain ResNet20 on CIFAR-10 is illustrated.

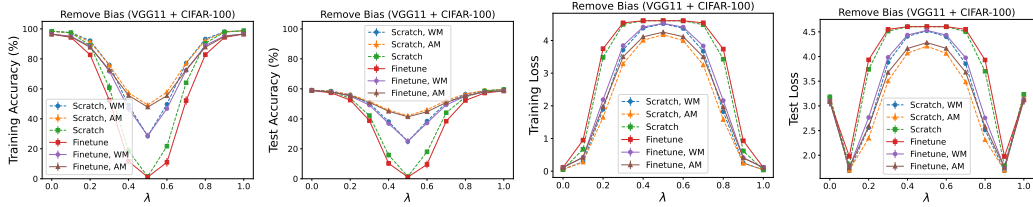


Figure 16: Training from scratch without biases vs. removing biases in a pre-trained model followed by fine-tuning. Linear interpolation between two VGG11 on CIFAR-100 is illustrated.

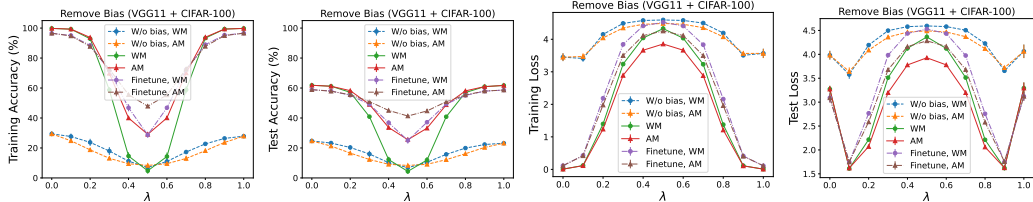


Figure 17: Removing biases in a pre-trained model followed by fine-tuning. Linear interpolation between two VGG11 on CIFAR-100 is illustrated.

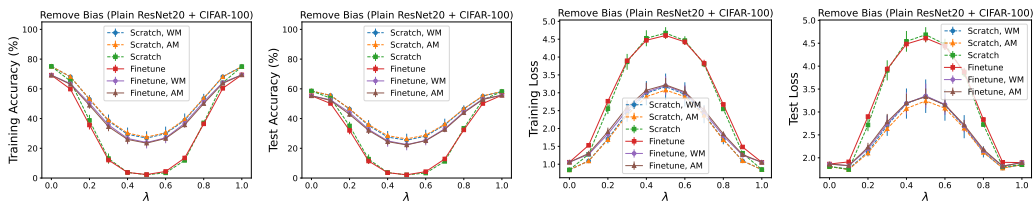


Figure 18: Training from scratch without biases vs. removing biases in a pre-trained model followed by fine-tuning. Linear interpolation between two plain ResNet20 on CIFAR-100 is illustrated.

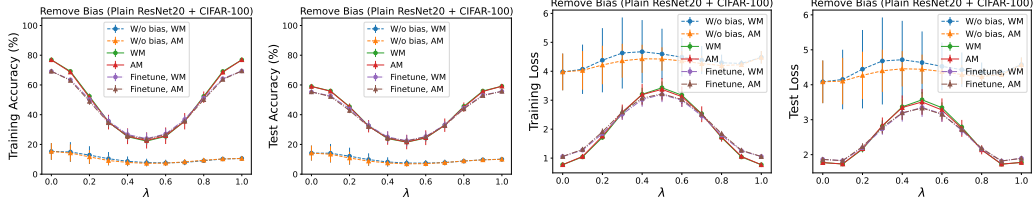


Figure 19: Removing biases in a pre-trained model followed by fine-tuning. Linear interpolation between two plain ResNet20 on CIFAR-100 is illustrated.

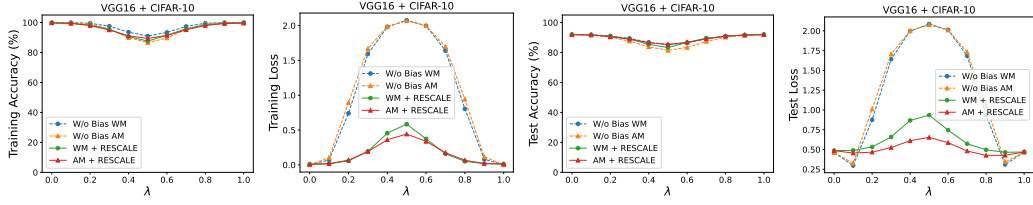


Figure 20: Removing biases vs. RESCALE. Linear interpolation between two VGG16 on CIFAR-10 is illustrated.

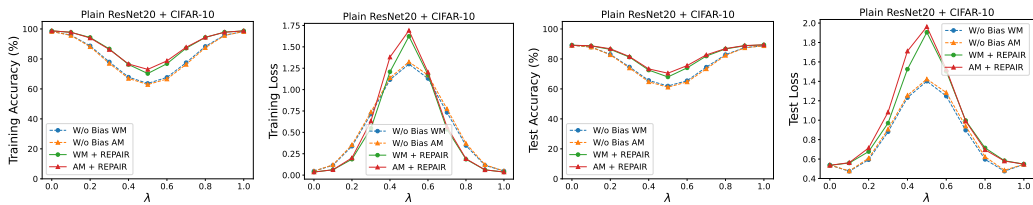


Figure 21: Removing biases vs. REPAIR. Linear interpolation between two plain ResNet20 on CIFAR-10 is illustrated.

G.3 Connection to [56]

This section elaborates on the relationship between re-basin and results in [56], as mentioned in Section 3.2.

[56] studies the monotonic linear interpolation (MLI) phenomenon: the loss and accuracy are typically monotonic on the line connecting a random initialization and the final SGD solution. This observation was previously regarded as evidence that the loss landscape around the SGD trajectory was nearly convex and hence the optimization was not too difficult [22], while opposite observations were recently shown in [17] where a long plateau often existed along this linear path on more advanced datasets. The results in [56] suggest that the plateau on the linear path can be simply attributed to reasons such as the bias terms, the network initialization scale, and the network depth, which don’t tell much about the optimization difficulty. Under their assumptions, the authors proved that the biases and weights in the model play a different role in the linear interpolation and that the model biases can largely affect the results (e.g., they can become worse). To demonstrate this, they proposed a *homogeneous interpolation* procedure when doing the interpolation (see Section 5 in [56]). Surprisingly, this simple change in the calculation removed the plateau and recovered the MLI.

We also tried this homogeneous interpolation in our experiments. As illustrated in Figures 22 and 23, this process also reduced the barrier. This observation suggested that the biases also play a significant role (at least for plain models) in linear interpolation between two independent solutions after matching. One analogy between the two scenarios is if we regard the poorly performed midpoint model as a model similar to the random initialization, the linear interpolation between two end models can be separated in the middle as the composition between two interpolations of the type “random init. – final solution”. Intriguingly, it was observed that the amount of barrier reduced by homogeneous interpolation was also similar to that bought by removing biases, and hence resembles that by re-normalization. As mentioned in the last section, another similarity is that homogeneous interpolation also can only affect the interpolation on the accuracy landscape. We believe these connections can illuminate a deeper understanding of the intrinsic principle under the hood, which is crucial for improving the practice.

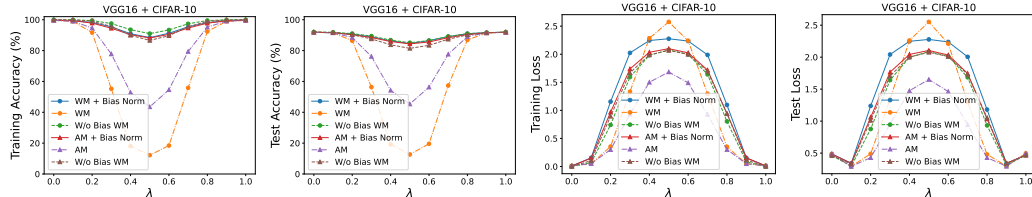


Figure 22: Linear interpolation between two VGG16 on CIFAR-10 is illustrated. The “bias norm” refers to the interpolation with Homogeneous normalization.

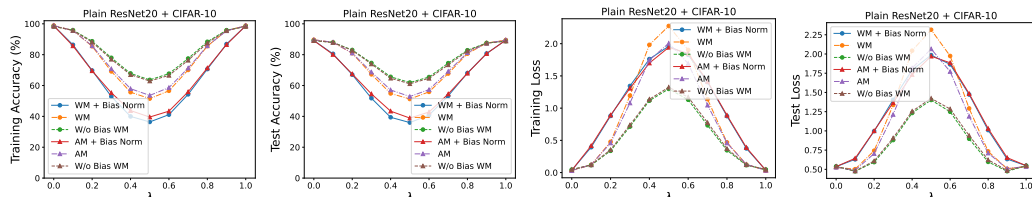


Figure 23: Linear interpolation between two plain ResNet20 on CIFAR-10 is illustrated. The “bias norm” refers to the interpolation with Homogeneous normalization.

G.4 Bonus: A Data-Independent Re-Normalization

In this section, we propose a novel data-independent re-normalization variant identified during our revisit to the re-normalization.

The proposed data-independent re-normalization consists of two key points: (1) recording the running statistics of the end models during training, and (2) turning on the training mode in the merged model when evaluating to record running statistics (perform normalization). The first step is already satisfied for models with BatchNorm. It can be easily achieved for other models by wrapping the layer in a customized module where the running statistics are recorded during training. This modification removes the necessity of data when setting goal running mean and variance in the interpolated model. After setting the target statistics, rather than recording statistics in the interpolated model by feeding training data, the model is directly employed for evaluation but in a training mode. This means that running statistics are automatically applied during evaluation. We observed that this approach could achieve comparable performance to the vanilla method, as shown in Tables 11 and 12, while exhibiting a distinct advantage in data independence. In addition, it was also found that several batches of data already sufficed when recording the statistics.

Table 11: Data-independent RESET, evaluated on VGG16 BN + CIFAR-10. The final test accuracy of the midpoint model is reported. Batch size is set as 128.

Variant	WM	AM
Original	88.74%	88.51%
Data Independent	86.59%	86.44%

Table 12: Data-independent REPAIR/RESCALE, evaluated on VGG16 LN + CIFAR-10. The final test accuracy of the midpoint model is reported. Batch size is set as 128.

Variant	WM		AM	
	REPAIR	RESCALE	REPAIR	RESCALE
Original	89.2%	87.27%	87.95%	84.27%
Data Independent	88.39%	86.2%	86.47%	83.16%

G.5 A Novel Post-Pruning Plug-In

Firstly, we provide the modified formulation of REPAIR used for pruning. Given the original model N and the pruned model N_p , REPAIR is applied to N_p to corrects the channel-wise pre-activation statistics for all channels $\{N_p^{(i,j)}\}$ in selected layers $\{N_p^{(i)}\}$ based on the corresponding channels $\{N^{(i,j)}\}$ from the original unpruned model:

$$\text{REPAIR: } \tilde{N}_p^{(i,j)}(x) \leftarrow \frac{\tilde{N}_p^{(i,j)}(x) - \mu_p^{(i,j)}}{\sigma_p^{(i,j)}} \cdot w^{(i,j)} + b^{(i,j)},$$

where x , $\tilde{N}_p^{(i,j)}(x)$ is the input and pre-activation of $N_p^{(i,j)}$, $w^{(i,j)} = \mu^{(i,j)}$ is the goal standard deviation, $b^{(i,j)} = \sigma^{(i,j)}$ is the goal activation mean, and $\mu^{(i,j)}$, $\sigma^{(i,j)}$ is the channel-wise mean and standard deviation of the layer output. The subscript refers to which model the statistics belong to, and the superscript (i, j) refers to the j -th channel in the i -th layer. RESET can be modified similarly.

We present additional results of pruning ResNet20, ResNet20 LN, VGG16 BN, VGG16 LN, and plain ResNet20 on CIFAR-10 and CIFAR-100 in Figure 24 and 25. Results of applying RESET and REPAIR to pruned ResNet50 and ConvNeXt-T are given in Figure 26. In all experiments, we follow the standard setup of [50] only to prune weights in all convolutional and linear layers. The first convolutional layer is ignored when pruning ResNet50 on ImageNet. Following [52], we pruned all the linear layers in the convNeXt-T model which account for most parameters. The code for all pruning experiments is adapted from [50] with merely several new lines of code for performing REPAIR and RESET, demonstrating the convenience when merging this technique with any existing pruning framework. Consequently, the same hyperparameters for pruning as [50] are adopted in this work. For instance, the fisher subsample and fisher mini-batch sizes for the WoodFisher pruner are set to 400 in CIFAR-10/CIFAR-100 pruning. For the model except ResNet50, results with sparsity rates of 10%, 20%, ..., 90%, 95%, and 99% are reported. For ResNet50, we prune the model up to a sparsity of 90%. Since the main objective of this work is not to highlight this novel post-pruning

technique, we only demonstrate its power in the one-shot pruning scenario, but the logic also applies to other pruning frameworks, such as structured pruning and gradual pruning. We regard this as a promising direction worthy of further exploration and leave this for future work. For pruning ResNet50 on ImageNet, a simple hyperparameter setting of the WoodFisher pruner is utilized, e.g., fisher subsample size = 80 and fisher mini-batch size = 100, to save computational cost and avoid interference. Although this restricts the performance of the pruner (e.g., the WoodFisher performs similarly to the global magnitude pruning), a significant improvement after RESET has already been shown in our results and should be universal after merely changing some hyperparameters. We leave the efforts towards improving the SOTA results for future work. Meanwhile, we noticed that the RESET in models with BatchNorm was already used in a few pruning literatures [38], but its direct impact on improving the final model performance hasn't been thoroughly investigated. We emphasize that, for instance, the significant improvement in one-shot pruning is valuable in cases where the local re-training cannot proceed, e.g., in some end devices in the context of federated learning [42]. Furthermore, using REPAIR in our work makes applying this strategy to a wider range of model architectures possible.

In [32], it was reported that feeding a small portion of data ($\sim 5,000$ examples) for statistics recording is already sufficient to guarantee the performance of REPAIR/RESET. In the context of pruning, we found that even one batch of data (64 in our pruning experiment) is often already enough. We provide one example of applying RESET with 64/128/258 samples to the pruned ResNet20 on CIFAR-10 in Figure 26. Note that this is both for the statistics recording in the unpruned model and the pruned model. For global magnitude pruning and layerwise magnitude pruning, one batch of data already suffices to produce a result almost the same as the complete RESET. This is particularly meaningful in resource-limited settings, especially considering its remarkable performance-boosting ability, which can yield comparable results to advanced pruning methods like WoodFisher, even when applied to simple magnitude pruning. It's also noteworthy that the additional BN parameters in REPAIR can be eliminated by merging them into the original layers, as discussed in the original paper [32]. In summary, this re-normalization technique is extremely lightweight as there are no additional parameters, and the computational cost is negligible.

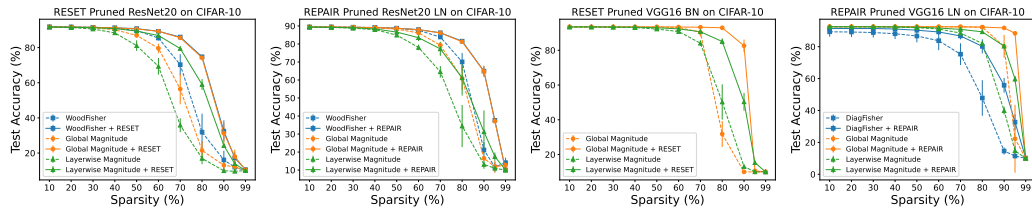


Figure 24: Apply REPAIR/RESET to pruned models on CIFAR-10. The diagonal-Fisher pruning performs poorly on VGG16 BN and is hence ignored here.

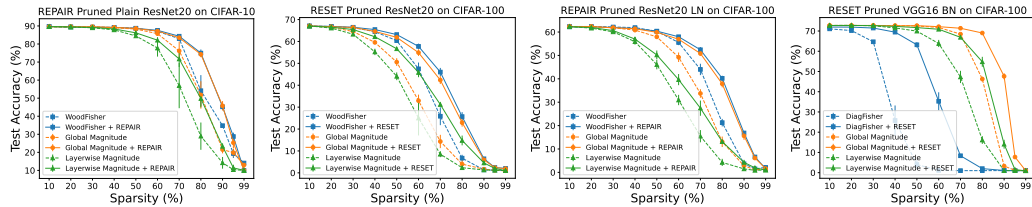


Figure 25: (A) Apply REPAIR to pruned plain ResNet20 on CIFAR-10. (B) & (C) & (D) Apply RESET/REPAIR to pruned models on CIFAR-100.

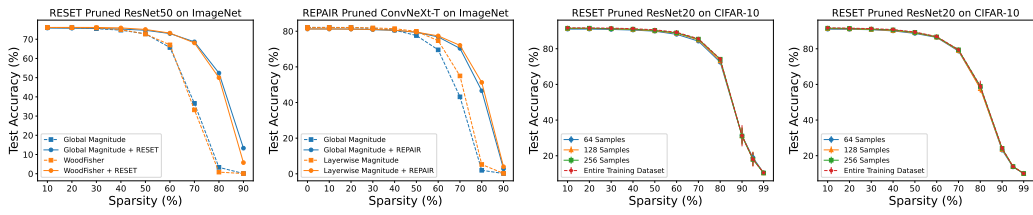


Figure 26: **(A)** Apply RESET to pruned ResNet50 on ImageNet. **(B)** Apply REPAIR to pruned ConvNeXt-T on ImageNet. **(C) & (D)** Compare the number of samples utilized in re-normalization after the global magnitude pruning ((C)) and layerwise magnitude pruning ((D)).

H Supplementary to “Rethinking Matching”

The section supplements Section 4 in the main paper.

H.1 Activation Collapse

This subsection provides results and discussions in support of Section 4.1.

Activation Statistics. Complete visualizations of the activation statistics in the midpoint model across different experiments are earlier provided in Figures 6, 7, 9 and 10, including VGG16, plain ResNet20, Fixup ResNet20 on CIFAR-10 and VGG11 on CIFAR-100. Activation statistics of each convolutional and linear layer in the end models and midpoint models are reported. These plots confirm that while the pre-ReLU activation statistics of the midpoint model were similarly restored by REPAIR or RESCALE regardless of matching, there were negligible improvements in post-ReLU activation statistics without matching. In this paper, we attributed this *activation collapse* issue to the increasing number of inactive neurons (i.e., output zeros) in the midpoint model when processing each sample, as illustrated in Figure 27. This phenomenon is pronounced in the early layers, but the converse phenomenon is observed in the later ones where zero activation decreases compared with the end models. We hypothesize that this is a consequence of the activation collapse in the early layers, which accumulates errors and creates noises in the deeper, resulting in more non-zero activation. For instance, we noticed that although applying RESCALE to the midpoint model without matching significantly recovered statistics in the later layers, the model performance didn’t improve, suggesting that extreme irregularity still existed. The impact of increasing learning rates on alleviating the activation collapse in some layers is shown in Table 13.

Learning Rate. Complete results of comparing different values of learning rate are shown in Figures 28 and 29. In all settings and for both weight matching and activation matching, the barrier keeps decreasing with a larger learning rate. We also provide all the interpolation plots in Figures 34, 35, 37, 38, 40, 41, 43 and 44. The complete VGG16 LN + MNIST results are provided in Figure 46.

We provide more details on the ablation experiment. After obtaining two pairs of solutions, one trained with large $lr = 0.1$ and the other with small $lr = 0.01$, we retrained the large lr solutions with $lr = 0.1$ for one more epoch to degrade their performances. Then we compare their interpolation results with the results between small lr solutions. As illustrated in Figures 36, 39, 42, and 45, in all settings and for both weight matching and activation matching, the large lr models still outperforms regarding the midpoint accuracy, though the end models already have a worse performance at this point.

When different learning rates are applied, we also investigate the midpoint performances before and after matching. We consider VGG16 BN, VGG16 LN, ResNet20 (4× width), ResNet20 LN (4× width) on CIFAR-10. As shown in Figures 30, 31, 32, and 33, there was an obvious improvement in the accuracy when matching was not performed, except a slight decrease in barrier in the ResNet20 (4× width) experiment. These results support our view that the improvement by larger learning rates is not trivially by the improved test accuracy in the end models.

Initialization Strategy. The effect of initialization when training with a small learning rate is illustrated in Figures 47 and 48. In particular, the same observation was drawn on ResNet20 LN.

Firstly, we describe the specific initialization strategies used in our experiments. For the Kaiming uniform initialization, we directly adopted the PyTorch [45] default. The Kaiming normal initialization is standard for training VGG, e.g., used in Torchvision. Specifically, for a 2D convolutional layer, the uniform initialization samples the weights and biases from the uniform distribution $U\left[\frac{-1}{\sqrt{k}}, \frac{1}{\sqrt{k}}\right]$, where $k = \text{num_in} \times \text{kernel_size}[0] \times \text{kernel_size}[1]$; while the normal initialization samples the weights from the Gaussian distribution $N(0, \frac{2}{k})$, where $k = \text{num_out} \times \text{kernel_size}[0] \times \text{kernel_size}[1]$, and sets the bias to 0. For a linear layer, the uniform initialization samples weights and biases from $U\left[\frac{-1}{\sqrt{k}}, \frac{1}{\sqrt{k}}\right]$, where $k = \text{num_in}$; while the normal initialization samples the weights from $N(0, 0.01)$ and sets bias to zero. This creates a larger variance at initialization for the normal initialization, which can be observed from the distance between two independently initialized models, as illustrated in Figures 4 and 49.

Below, we provide an analysis to understand the impact of the initialization strategy. After careful examination, we found that Kaiming initialization samples elements from a distribution with a larger

variance, and hence, the initial distance between two independent models is larger. We report the ℓ_2 distance between independent models during training in Figure 49. We hypothesized that When trained with small learning rates, models tend to converge towards solutions close to the initialization [10], maintaining the large distance between the final solutions, making it challenging or even impossible to discover a permutation for effective matching. On the other hand, the implicit bias of large learning rates mitigates the impact of initialization.

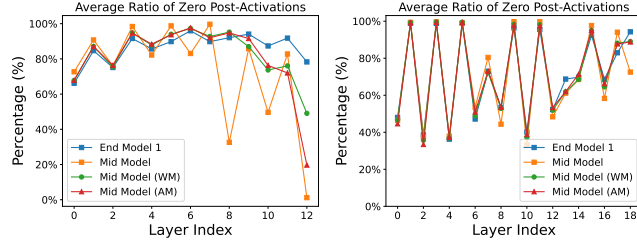


Figure 27: Percentage of zero post-activation per forward calculation in each layer. **Left two:** VGG16 + CIFAR-10. **Right two:** Plain ResNet20 + CIFAR-10.

Table 13: Large learning rates alleviate the activation collapse in some layers of the post-matching midpoint model, evaluated on VGG16 + CIFAR-10. We calculate the portion of previously activated neurons that turn inactive on average in each layer per sample. The best results are in bold.

Variant	Lr = 0.01	Lr = 0.1
Conv_4	70.51%	62.18%
Conv_6	67.47%	57.33%

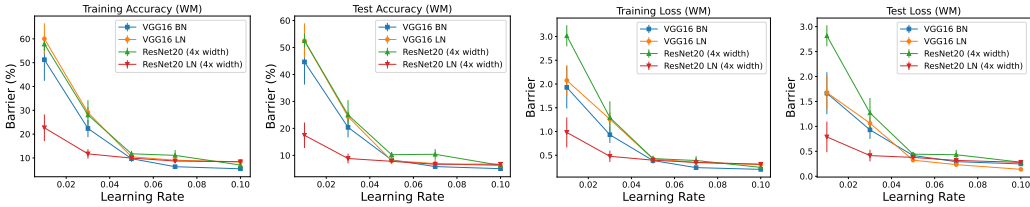


Figure 28: Barrier between two independent models trained on CIFAR-10. Weight matching is applied.

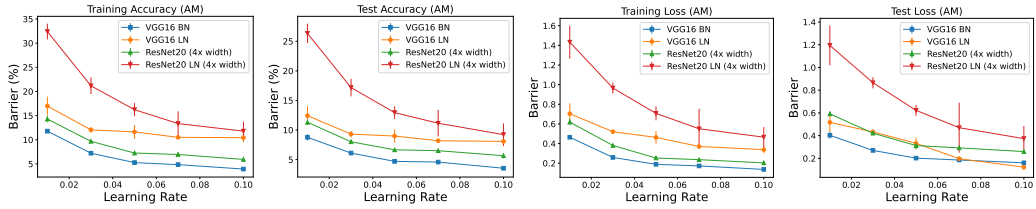


Figure 29: Barrier between two independent models trained on CIFAR-10. Activation matching is applied.

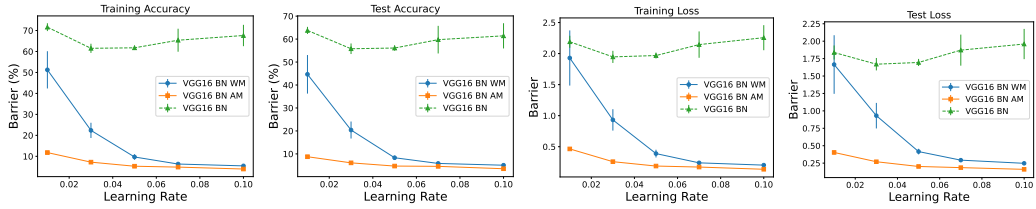


Figure 30: Barrier between two independent VGG16 BN trained on CIFAR-10 before/after matching.

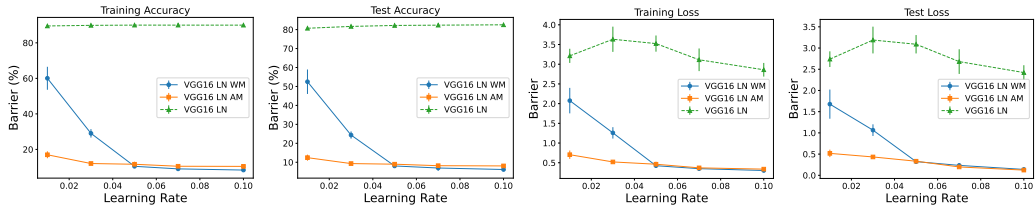


Figure 31: Barrier between two independent VGG16 LN trained on CIFAR-10 before/after matching.

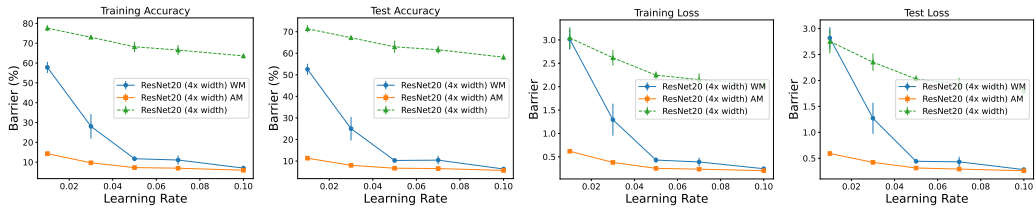


Figure 32: Barrier between two independent ResNet20 (4x width) trained on CIFAR-10 before/after matching.

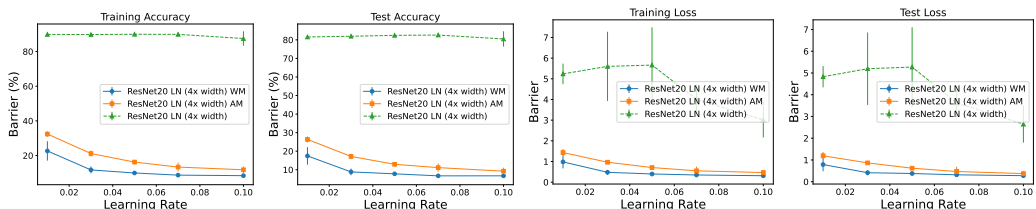


Figure 33: Barrier between two independent ResNet20 LN (4x width) trained on CIFAR-10 before/after matching.

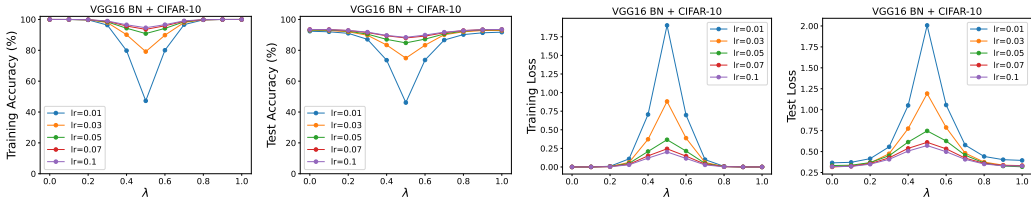


Figure 34: Benefit brought by training with large learning rates. Linear interpolation plot between two independent VGG16 BN trained on CIFAR-10. Weight matching is applied.

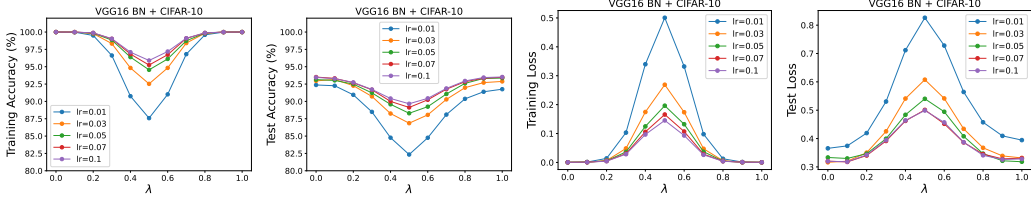


Figure 35: Benefit brought by training with large learning rates. Linear interpolation plot between two independent VGG16 BN trained on CIFAR-10. Activation matching is applied.

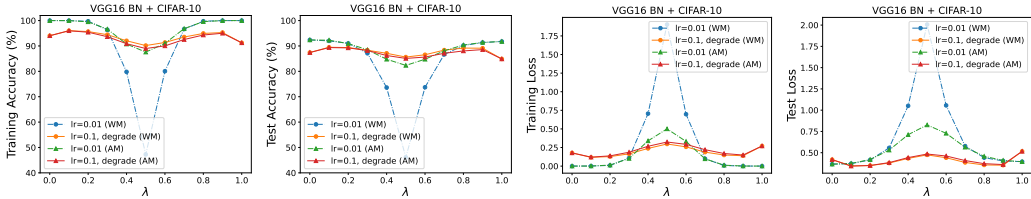


Figure 36: Learning rate ablation, VGG16 BN + CIFAR-10. The “degrade” refers to the interpolation after retraining the solution for one epoch.

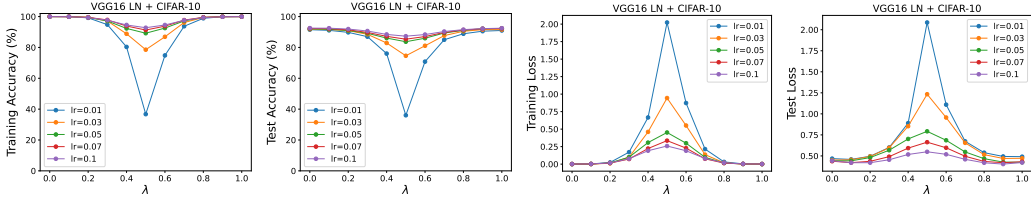


Figure 37: Benefit brought by training with large learning rates. Linear interpolation plot between two independent VGG16 LN trained on CIFAR-10. Weight matching is applied.

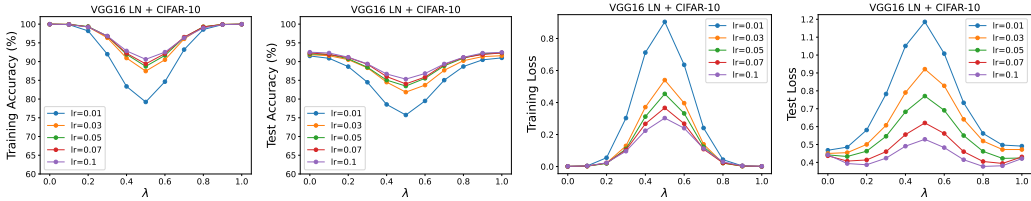


Figure 38: Benefit brought by training with large learning rates. Linear interpolation plot between two VGG16 LN trained on CIFAR-10. Activation matching is applied.

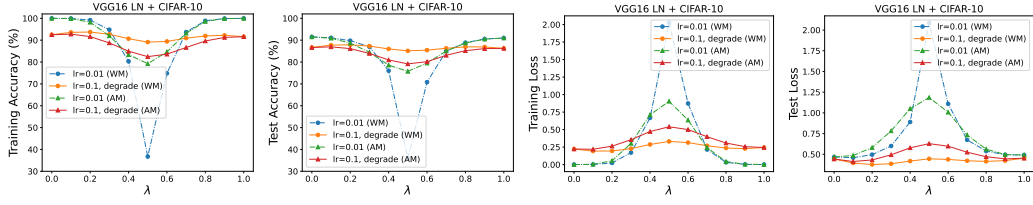


Figure 39: Learning rate ablation, VGG16 LN + CIFAR-10. The “degrade” refers to the interpolation after retraining the solution for one epoch.

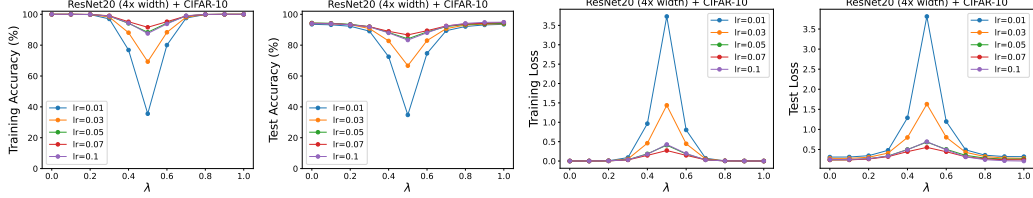


Figure 40: Benefit brought by training with large learning rates. Linear interpolation plot between two ResNet20 ($4 \times$ width) trained on CIFAR-10. Weight matching is applied.

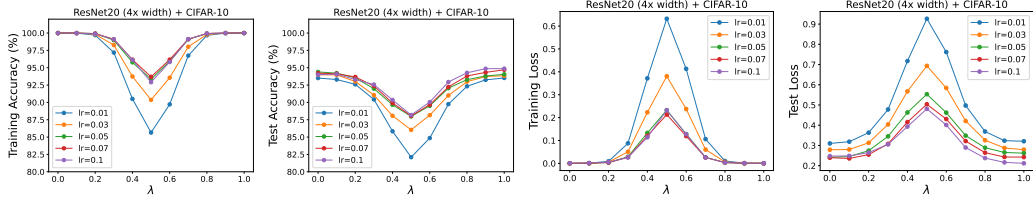


Figure 41: Benefit brought by training with large learning rates. Linear interpolation plot between two independent ResNet20 ($4 \times$ width) trained on CIFAR-10. Activation matching is applied.

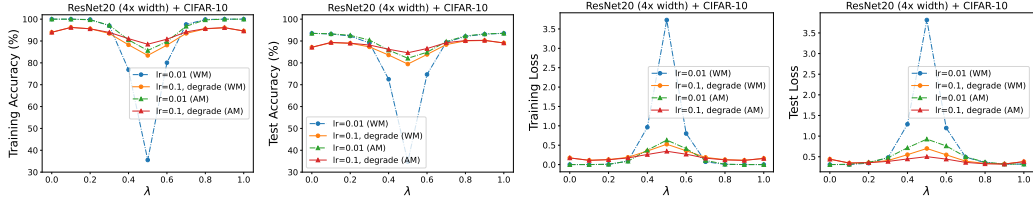


Figure 42: Learning rate ablation, ResNet20 ($4 \times$ width) + CIFAR-10. The “degrade” refers to the interpolation after retraining the solution for one epoch.

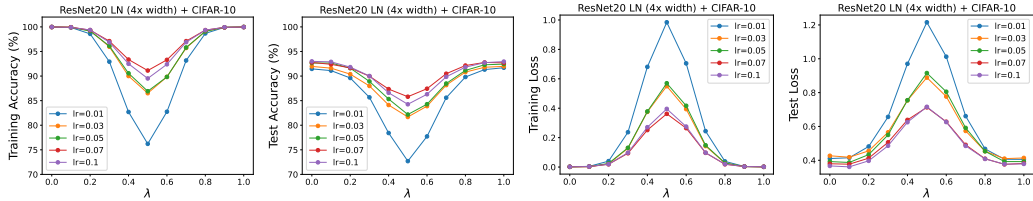


Figure 43: Benefit brought by training with large learning rates. Linear interpolation plot between two independent ResNet20 LN ($4 \times$ width) trained on CIFAR-10. Weight matching is applied.

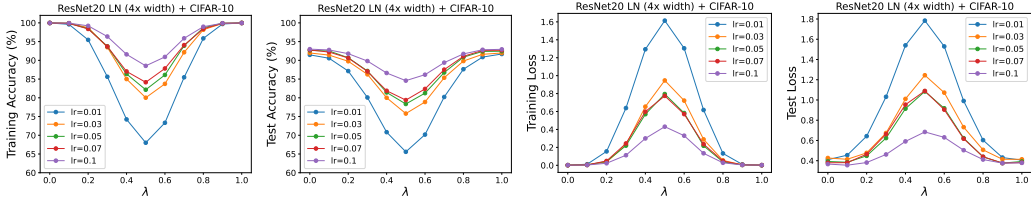


Figure 44: Benefit brought by training with large learning rates. Linear interpolation plot between two independent ResNet20 LN ($4 \times$ width) trained on CIFAR-10. Activation matching is applied.

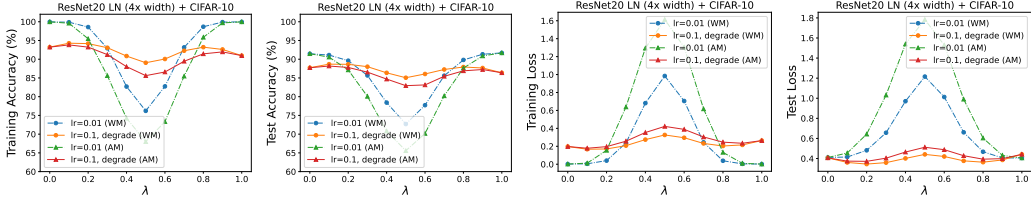


Figure 45: Benefit brought by training with large learning rates. Learning rate ablation, ResNet20 LN ($4 \times$ width) + CIFAR-10. The “degrade” refers to the interpolation after retraining the solution for one epoch.

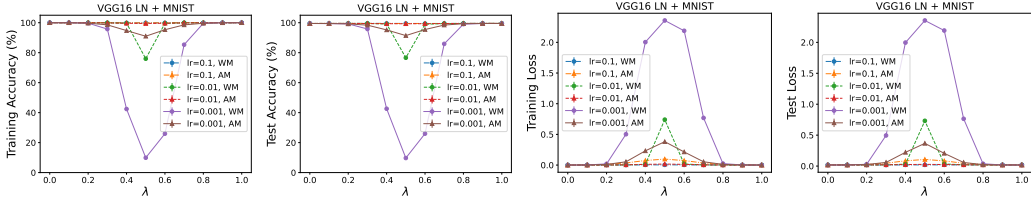


Figure 46: Linear interpolation plot between two independent VGG16 LN trained on MNIST.

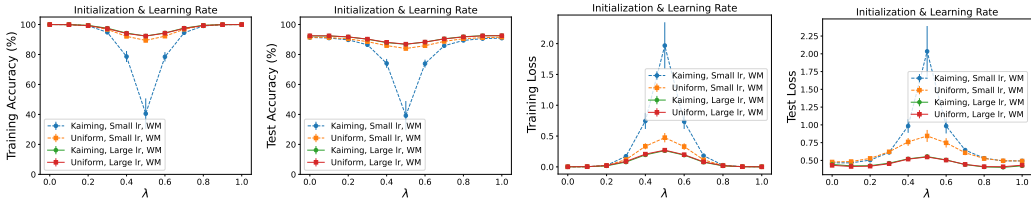


Figure 47: Impact of initialization. Linear interpolation plot between two independent VGG16 LN trained on CIFAR-10. Kaiming: Kaiming normal initialization. Uniform: Kaiming uniform initialization.

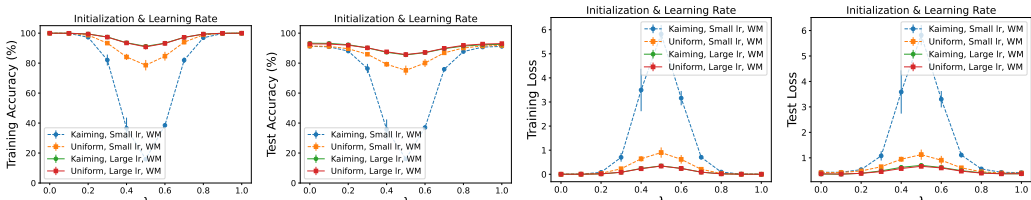


Figure 48: Impact of initialization. Linear interpolation plot between two independent ResNet20 LN ($4 \times$ width) trained on CIFAR-10. Kaiming: Kaiming normal initialization. Uniform: Kaiming uniform initialization.

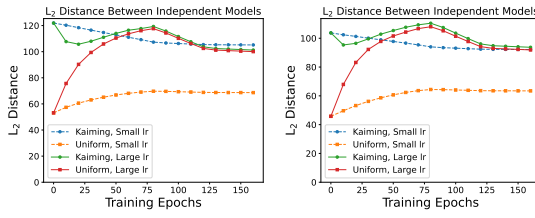


Figure 49: Distance between independent models trained on CIFAR-10. “Kaiming” refers to the Kaiming normal initialization and “Uniform” refers to the Kaiming uniform initialization. **Left:** VGG16 LN. **Right:** ResNet20 LN (4× width).

H.2 Magnitude Collapse

This subsection provides results and discussions in support of Section 4.2.

Complete Results. We provide the complete visualization of our results below. The illustration of magnitude collapse is in Figure 50. We provide the interpolation plots when varying the strength of weight decay in Figures 51, 53, and 55. For the ablation experiment, we retrain the small $wd = 1e - 4$ solutions for one more epoch with $wd = 5e - 4$. Complete results are shown in Figures 52, 54, and 56. Lastly, Figure 60 provides complete results comparing RESCALE and REPAIR when different strength of weight decay is utilized.

We also report the midpoint performances before and after matching. We consider VGG16 BN, VGG16 LN, ResNet20, and ResNet20 LN on CIFAR-10, shown in Figure 57. In all cases, there was no obvious improvement in accuracy when matching was not performed, supporting our view that the improvement by stronger weight decay is not trivially by the improved test accuracy in the end models.

Moreover, we showcase the compression effect of weight decay regularization in Figures 58 and 59. The density plots of the parameter magnitude and activation statistics are reported. The activation statistics are averaged in each channel.

Theoretical View. Firstly, we provide details of the expectation calculation shown in Section 4.2.

Proposition H.1. *Suppose x, y is independently drawn from the uniform distribution $U(\mu - \sigma, \mu + \sigma)$ ($\sigma > \mu > 0$), then we have*

$$\begin{aligned}
\mathbb{E}[|x| + |y| - |x + y|] &= \frac{1}{4\sigma^2} \int_{\mu-\sigma}^{\mu+\sigma} \int_{\mu-\sigma}^{\mu+\sigma} |x| + |y| - |x + y| dx dy \\
&= \frac{1}{4\sigma^2} \left(\int_0^{\mu+\sigma} \int_{\mu-\sigma}^0 |x| + |y| - |x + y| dx dy \right. \\
&\quad \left. + \int_{\mu-\sigma}^0 \int_0^{\mu+\sigma} |x| + |y| - |x + y| dx dy \right) \\
&= \frac{1}{2\sigma^2} \int_0^{\mu+\sigma} \int_{\mu-\sigma}^0 -x + y - |x + y| dx dy \quad (\text{by symmetry}) \\
&= \frac{1}{2\sigma^2} \left(\int_0^{\sigma-\mu} \int_{\mu-\sigma}^{-y} (-x + y + x + y) dx dy \right. \\
&\quad \left. + \int_0^{\sigma-\mu} \int_{-y}^{\sigma+\mu} (-x + y - x - y) dx dy \right) \\
&\quad + \int_{\sigma-\mu}^{\mu+\sigma} \int_{\mu-\sigma}^0 (-x + y - x - y) dx dy \\
&= \frac{(\sigma + 2\mu)(\sigma - \mu)^2}{3\sigma^2}.
\end{aligned}$$

Secondly, we elaborate our statement in Section 4.2 which is based on results of [15]. The main results we utilized is [15, Theorem 5.4]:

Theorem H.2. [15, Theorem 5.4] *Under [15, Assumptions 7 and 8], given $\epsilon > 0$, if $em_0 \geq 5$ there exists minimal widths $\tilde{m}_1, \dots, \tilde{m}_L$ such that if $\eta^{-k_0} \geq m_1 \geq \tilde{m}_1, \dots, \eta^{-k_{L-1}} \geq m_L \geq \tilde{m}_L$, [15, Property 1] is verified at the last hidden layer L for $E_L = 1, E_L = \epsilon^2$. Moreover, $\forall \ell \in [L], \exists T'_\ell$ which does only depend on L, e, ℓ , such that one can define recursively \tilde{m}_ℓ as*

$$\tilde{m}_\ell = \tilde{\mathcal{O}} \left(\frac{T'_\ell}{\epsilon} \right)^{k_{\ell-1}} = \tilde{\mathcal{O}} \left(\frac{T'_\ell}{\epsilon} \right)^{em_{\ell-1}}$$

where $\tilde{m}_0 = m_0$. Moreover there exists permutations of hidden layers $1, \dots, L$ of network B s.t. $\forall t \in [0, 1]$, with Q -probability at least $1 - \delta_Q$:

$$\mathbb{E}_P \left[\mathcal{L} \left(\hat{f}_{M_t}(x), y \right) \right] \leq t \mathbb{E}_P \left[\mathcal{L} \left(\hat{f}_A(x), y \right) \right] + (1 - t) \mathbb{E}_P \left[\mathcal{L} \left(\hat{f}_B(x), y \right) \right] + \frac{4\sqrt{m_{L+1}}}{\sqrt{e}\delta_Q^2} \epsilon. \quad (3)$$

Since the original paper has many intermediate results and assumptions up to this theorem, we recommend that readers read the original paper for more details. Here, we briefly introduce symbols in this theorem, Equation (3) provides a bound on the expectation of the post-matching barrier, measured by the loss function \mathcal{L} . The end models are two MLPs of $L + 1$ layers, denoted as A and B . $M_t = t \cdot A + (1 - t) \cdot B$ is the merged model. m_1, \dots, m_L denotes the width of each layer. In particular, the input dimension is denoted as m_0 . Theorem H.2 considers a low-dimensional scenario where each layer has an intrinsic width $\tilde{m}_\ell \leq m_\ell$. An important concept in the derivation of [15] is the approximation of the dimension of the support of the underlying weights distribution, defined as k_ℓ , where $k_\ell \leq \tilde{m}_\ell$. Further, the ratio $\frac{k_\ell}{\tilde{m}_\ell} \leq 1$ is denoted as e_ℓ .

In [15], this theorem further assumes that the weights at layer ℓ are initialized i.i.d from the multivariate Gaussian $\mu_\ell = \mathcal{N}(0, \Sigma^{\ell-1})$ with

$$\Sigma^{\ell-1} := \text{Diag} \left(\lambda_1^\ell I_{p_{\ell-1}}, \lambda_2^\ell I_{p_{\ell-1}}, \dots, \lambda_{\tilde{m}_{\ell-1}}^\ell I_{p_{\ell-1}} \right),$$

where $\frac{1}{m_{\ell-1}} \frac{1}{e_\ell} = \frac{1}{m_{\ell-1}} \frac{\tilde{m}_{\ell-1}}{k_{\ell-1}} \geq \lambda_1^\ell \geq \lambda_2^\ell \geq \dots \geq \lambda_{\tilde{m}_{\ell-1}}^\ell$. The [15, Assumption 8] then assumes the existence of a universal e across the layers:

$$\text{Assumption H.3. [15, Assumption 8]} \exists \eta, e \in (0, 1), \forall \ell \in [L], \frac{\sqrt{\sum_{j=k_{\ell-1}}^{\tilde{m}_{\ell-1}} \lambda_j^\ell}}{4\sqrt{\sum_{j=1}^{k_{\ell-1}} \lambda_j^\ell}} \leq \eta, \frac{k_{\ell-1}}{\tilde{m}_{\ell-1}} = e.$$

This assumption states an approximately low dimensionality of weights in the network. From here, if we limit the weights in a small region by decreasing the variance λ_i^ℓ , then a more accurate estimation of the intrinsic dimension can be taken, i.e., e can be taken closer to 1. Recall that the bound on the barrier provided in Theorem H.2 is $\frac{4\sqrt{m_{L+1}}}{\sqrt{e}\delta_Q^2} \epsilon$. Hence, increasing the value of e indeed lowers this bound, supporting the impact of weight decay reported in Section 4.2.

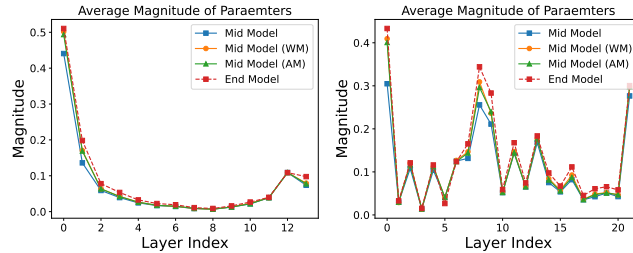


Figure 50: Average magnitude of parameters in each layer. **Left two:** VGG16 + CIFAR-10. **Right two:** Plain ResNet20 + CIFAR-10.

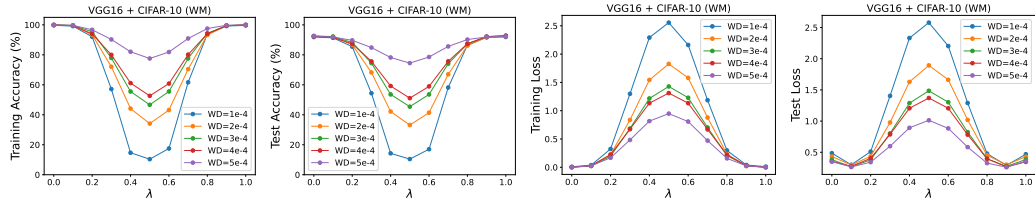


Figure 51: Benefit brought by training with large weight decay. Linear interpolation between independent VGG16 trained on CIFAR-10. Weight matching is applied.

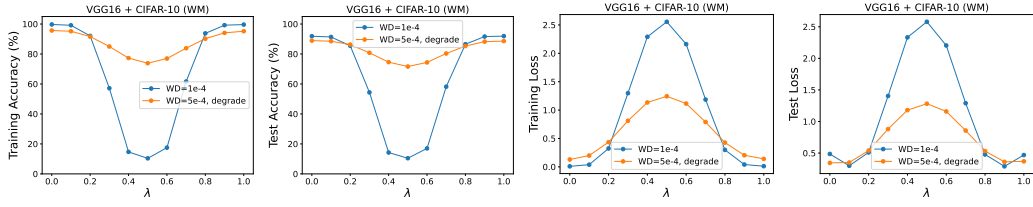


Figure 52: Weight decay ablation, VGG16 + CIFAR-10. Weight matching is applied. The “degrade” refers to the interpolation after retraining the solution for one epoch.

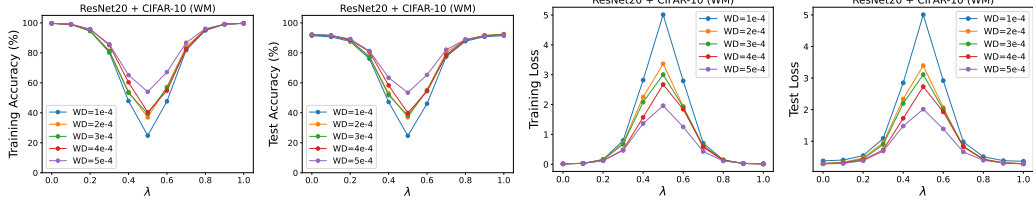


Figure 53: Benefit brought by training with large weight decay. Linear interpolation between independent ResNet20 trained on CIFAR-10. Weight matching is applied.

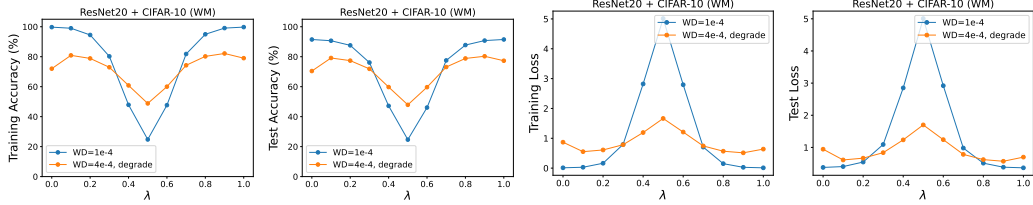


Figure 54: Weight decay ablation, ResNet20 + CIFAR-10. Weight matching is applied. The “degrade” refers to the interpolation after retraining the solution for one epoch.

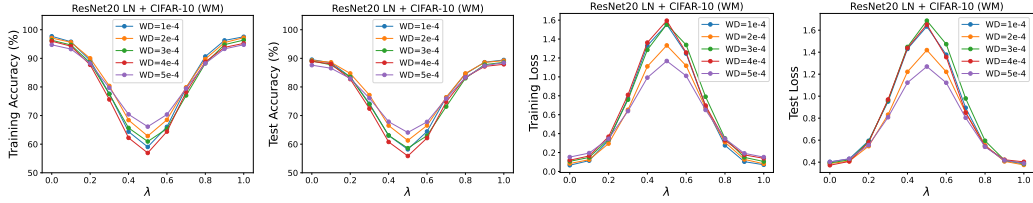


Figure 55: Benefit brought by training with large weight decay. Linear interpolation between independent ResNet20 LN trained on CIFAR-10. Weight matching is applied.

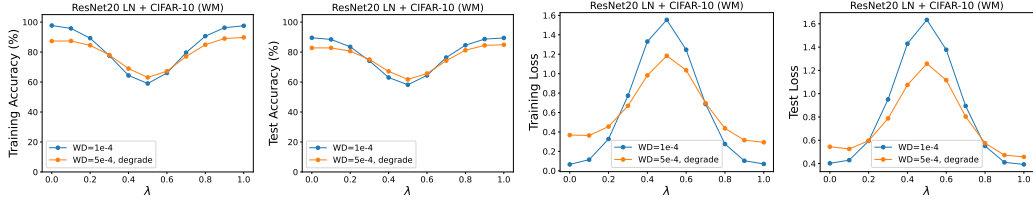


Figure 56: Weight decay ablation, ResNet20 LN + CIFAR-10. Weight matching is applied. The “degrade” refers to the interpolation after retraining the solution for one epoch.

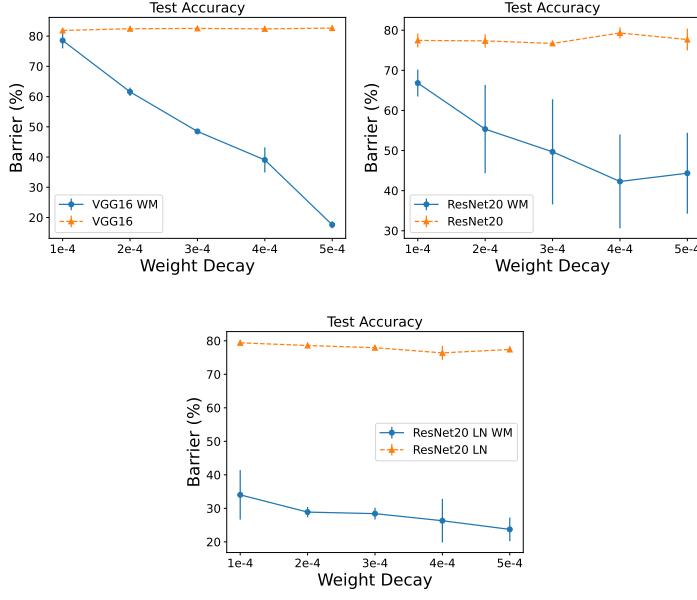


Figure 57: Barrier between two independently trained models on CIFAR-10 before/after the weight-matching.

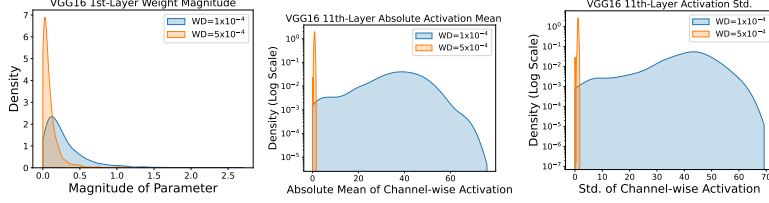


Figure 58: The compression effect brought by weight decay, VGG16 + CIFAR-10. Density plots are reported.

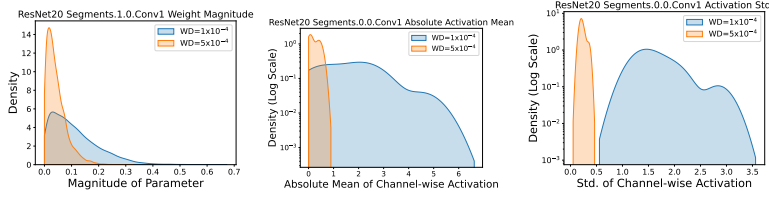


Figure 59: The compression effect brought by weight decay, ResNet20 + CIFAR-10. Density plots are reported.

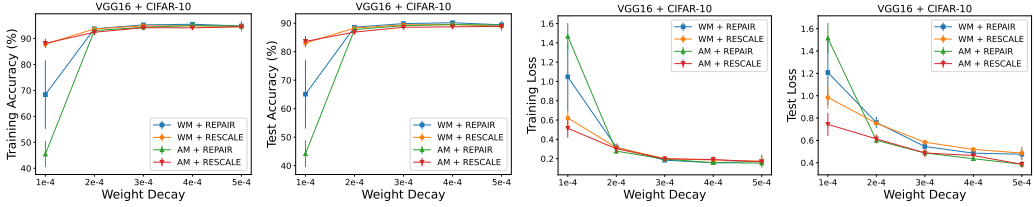


Figure 60: Improve REPAIR by RESCALE. The barrier between two VGG16 on CIFAR-10 is illustrated.